2

3

Antarctic ocean and sea ice response to ozone depletion: a two

timescale problem

David Ferreira, * John Marshall,

Department of Earth, Atmospheric and Planetary Sciences, Massachusetts Institute of Technology, Cambridge, MA

CECILIA M. BITZ,

Atmospheric Sciences Department, University of Washington, Seattle, WA

Susan Solomon, and Alan Plumb

Department of Earth, Atmospheric and Planetary Sciences, Massachusetts Institute of Technology, Cambridge, MA

E-mail: d.g.ferreira@reading.ac.uk

^{*}Corresponding author address: David Ferreira, now at the Department of Meteorology, University of Reading, PO Box 243, Reading, RG6 6BB, UK.

ABSTRACT

6

The response of the Southern Ocean to a repeating seasonal cycle of ozone loss is studied in two coupled climate models and found to comprise both fast and slow processes. The fast response is similar to the inter-annual signature of the Southern Annular Mode (SAM) on Sea Surface Temperature (SST), on to which the ozone-hole forcing projects in the summer. 10 It comprises enhanced northward Ekman drift inducing negative summertime SST anomalies 11 around Antarctica, earlier sea ice freeze-up the following winter, and northward expansion 12 of the sea ice edge year-round. The enhanced northward Ekman drift, however, results 13 in upwelling of warm waters from below the mixed layer in the region of seasonal sea ice. 14 With sustained bursts of westerly winds induced by ozone-hole depletion, this warming from below eventually dominates over the cooling from anomalous Ekman drift. The resulting slow-timescale response (years to decades) leads to positive SST anomalies around Antarc-17 tica and ultimately a reduction in sea-ice cover year-round. This two-timescale behavior rapid cooling followed by slow but persistent warming - is found in the two coupled models 19 analysed, one with an idealized geometry, the another a complex global climate model with 20 realistic geometry. Processes that control the timescale of the transition from cooling to 21 warming, and their uncertainties are described. Finally we discuss the implications of our results for rationalizing previous studies of the effect of ozone-hole on SST and sea-ice extent.

1. Introduction

25

few decades, with the pattern of decadal change closely resembling the positive phase of the Southern Annular Mode (SAM). Throughout the troposphere, pressure has trended down-27 ward south of 60°S and upward between 30 and 50°S in summer (Thompson and Solomon 28 2002; Marshall 2003; Thompson et al. 2011). This pattern of pressure change is associated 29 with a poleward shift of the westerly winds. These circulation trends have been attributed 30 in large part to ozone depletion in the stratosphere over Antarctica (Gillet and Thompson 31 2003; Marshall et al. 2004a; Polyani et al. 2011). During the same period, an expansion of 32 the Southern Hemisphere sea ice cover has been observed, which most studies find to be 33 significant (Zwally et al. 2002; Comiso and Nushio 2008; Turner et al. 2009). This expansion is observed in all seasons but is most marked in the fall (March-April-May). This is in 35 stark contrast with the large decrease of Arctic sea ice coverage observed over recent decades (Turner et al. 2009). 37 The ozone-driven SAM and sea ice trends could be related to one-another. However, 38 coupled climate models consistently show a warming of the SO surface and sea ice loss (in 39 all seasons) in response to ozone depletion (Sigmond and Fyfe 2010; Bitz and Polyani 2012; 40 Smith et al. 2012; Sigmond and Fyfe 2014). These studies concluded that the ozone hole did not contribute significantly to the expansion of the SO sea ice cover over the last three 42 decades (see also review by Previdi and Polyani 2014). This leaves us with an even bigger question: how could the SO sea ice cover increase in the face of both ozone depletion and global warming if both processes induce loss? The quandary is further complicated by the correlation between the SAM and ocean/sea ice variability found in both observations and models (Watterson 2000; Hall and Visbeck 2002; Sen Gupta and England 2006; Ciasto and Thompson 2008). Interannual variability in the SAM has a robust Sea Surface Temperature (SST) signature: a dipole in the meridional direction with a strong zonal symmetry. For a positive phase of the SAM, SST cools around Antarctica (south of about 50°S) and warms

The atmospheric circulation over the Southern Ocean (SO) has changed over the past

around 40°S. This response is understood as one that is mainly forced by Ekman currents and to a lesser extent air-sea fluxes (i.e. mixed layer dynamics). A positive phase of the 52 SAM is also associated with sea ice expansion at all longitudes except in the vicinity of Drake Passage (Lefebvre et al. 2004; Sen Gupta and England 2006; Lefebvre and Goosse 2008). Although difficult to measure, the Southern Ocean sea ice cover as a whole appears to increase slightly following a positive SAM. If this were the only important process at work, then one would expect a positive SAM-like atmospheric response to ozone depletion to drive SST cooling and sea ice expansion around Antarctica (and a SST warming around 40°S) in the long term. This scenario is reinforced by the clear resemblance between the pattern of sea ice concentration trends and the pattern of the sea ice response to a positive 60 SAM. Following this chain of thought, Goosse et al. (2009) pointed to the ozone-driven SAM changes as the main driver of the observed SO sea ice expansion. This behavior however 62 contradicts results from coupled climate models. 63

In this study, we attempt to reconcile the expectations from the aforementioned observed 64 SAM/SST correlations with those from coupled modeling studies including a representation 65 of ozone depletion. In particular, we compute the transient ocean response to a step func-66 tion in ozone depletion, but one that includes the seasonal cycle of depletion, in two coupled climate models, the MITgcm and CCSM3.5. As we shall see, this exposes the elemental processes and timescales at work. The approach, in direct analogy to the Climate Response Functions (CRFs) to Greenhouse gas forcing, is described in general terms in Marshall et al. (2014). We find that the SST response to ozone depletion is made up of two phases in both models (as summarized in the schematic in Fig. 1): a (fast) dipole response with a cooling around Antarctica (consistent with SAM/SST correlations on interannual timescales), 73 followed by a slow warming at all latitudes south of 30°S. This warming eventually leads 74 to a sign reversal of the SST response around Antarctica, and a switch to a positive SST 75 response throughout the SO, consistent with previous coupled GCM experiments. 76

Concomitant with SST fluctuations around Antarctica, our models display increases in

77

response of SST and sea ice in our models is consistent with the conclusions of previous authors. The short term response, however, suggests that ozone depletion may have contributed to the observed sea ice expansion of the last decades (see Marshall et al. 2014). The period during which sea ice could expand in response to ozone depletion depends on the processes that control the timescale of the SST and sea ice reversal. While the reversal occurs in both models, they exhibit a rather disparate timescale of transition from warming to cooling. Reasons for these differences are discussed.

Our paper is set out as follows. In section 2, the coupled GCM set-ups and experimental
designs are described. The ocean and sea ice responses to an abrupt ozone depletion and their
mechanism in the MITgcm and in CCSM3.5 are described in section 3 and 4, respectively.
Using a simple analytical model, in section 5 we identify key processes that account for the
different timescales in the two coupled GCMs. Finally, conclusions are given in section 6.

$_{\scriptscriptstyle{91}}$ 2. Coupled model set-ups

a. The MITqcm

We use the MITgcm in a coupled ocean-atmosphere-sea ice simulation of a highly idealized Earth-like Aquaplanet. Geometrical constraints on ocean circulation are introduced through "sticks" which extend from the top of the ocean to its flat bottom (Marshall et al. 2007; Enderton and Marshall 2009; Ferreira et al. 2010) but present a vanishingly small land surface area to the atmosphere above. In the "Double-Drake" configuration employed here, two such sticks separated by 90° of longitude extend from the North Pole to 35°S, defining a small basin and a large basin in the northern hemisphere and a zonally re-entrant Southern ocean. There is no land mass at the South Pole.

The atmospheric model resolves synoptic eddies, has a hydrological cycle with a representation of convection and clouds, a simplified radiation scheme and an atmospheric boundary

layer scheme (following Molteni 2003). The atmosphere is coupled to an ocean and a thermo-103 dynamic sea-ice model (due to Winton 2000) driven by winds and air-sea heat and moisture 104 fluxes. In the ocean, effects of mesoscale eddies are parametrized as an advective process 105 (Gent and McWilliams 1990) and an isopycnal diffusion (Redi 1982) using an eddy trans-106 fer coefficient of 1200 m² s⁻¹. Convection is parameterized as described in Klinger et al. 107 (1996). The coupled model is integrated forward using the same dynamical core (Marshall 108 et al. 1997a,b, 2004b) on the conformal cubed sphere (Adcroft et al. 2004). In calcula-109 tions presented here, present-day solar forcing is employed, including a seasonal cycle, with 110 present-day levels of greenhouse gas forcing. More details can be found in the appendix.

Despite the idealized continents, Double-Drake's climate has many similarities with to-112 day's Earth (Ferreira et al. 2010). Deep water is formed in the northern part of the narrow 113 Atlantic-like basin and is associated with a deep overturning circulation extending into the 114 Southern Ocean where is upwells isopycnally under the combined action of surface winds and 115 (parameterized) eddies. In contrast, the wide, Pacific-like basin is primarily wind driven. A 116 vigorous current, analogous to the Antarctic Circumpolar Current (ACC) develops in the 117 Southern Hemisphere in thermal wind balance with steep outcropping isopycnals. The sea 118 ice cover is perennial poleward of 75°S, but expands seasonally to about 65°S in September 119 (an increase of about 13.5 millions km² in sea ice area), similar to today's seasonal variations 120 in the Southern Ocean (e.g. Parkinson and Cavalieri 2012). In accord with observations, the 121 simulated ocean stratification south of the ACC is controlled by salinity with temperature 122 increasing at depth (notably because of the seasonal cycle of sea ice). This temperature in-123 version will turn out to be a central factor controlling the rate of subsurface warming under 124 seasonal sea ice found in response to SAM forcing. 125

Ozone is not explicitly computed in the model, but its shortwave absorption in the lower troposphere is represented (the model includes a single layer representing the lower stratosphere). Our "ozone hole" perturbation is introduced by reducing the ozone-driven shortwave absorption south of 60°S in this layer. The imposed ozone reduction is close to

130 100% at the Oct/Nov boundary as observed in the lower stratosphere but is tapered down
131 to 20% in spring (i.e. there is a minimum ozone depletion of 20% throughout the year).
132 This perturbation is comparable to that observed in the heart of the ozone hole during the
133 mid-to-late 90s (e.g. Solomon et al. 2007). The same perturbation is repeated every year.
134 Note also that the ozone radiative perturbation is scaled by the incoming solar radiation and
135 disappears during the polar night at high-latitudes.

The forced response is computed as the difference between the ensemble-average of the perturbed runs and the climatology of a 300 years long control run. Twenty 40-year long simulations with independent initial conditions (in both ocean and atmosphere) taken from the control run are carried out and monthly-mean outputs taken. Eight of those are integrated up to 350 years, by which point the coupled system approaches a new equilibrium.

Although our atmospheric model is simplified, it produces an atmospheric response to 141 ozone depletion which is rather similar to that found in more complex atmospheric and 142 coupled GCMs (e.g. Gillet and Thompson 2003; Sigmond et al. 2010; Polvani et al. 2011): 143 pressure decreases poleward of 50°S and increases in the 50-20°S band during the sum-144 mer. This is illustrated in Fig. 2 where the geopotential height at 500 mb is plotted. The 145 geopotential response vanishes during the winter months. There is an associated strength-146 ening/weakening of the westerly wind around 50/30°S, as shown in Fig. 5. The amplitude 147 of the anomaly, ± 40 m at 500 mb, is also comparable to those obtained in other studies in 148 response to a mid-1990s ozone depletion (Gillet and Thompson 2003). At the surface, the westerly wind stress anomaly is order 0.02 N m⁻² at its summer peak corresponding to a sea 150 level pressure response of ± 3 mb, both comparable to those found by Sigmond et al. (2010) 151 and Polvani et al. (2011). 152

Note that, as in other GCMs, the atmospheric response to ozone depletion strongly projects on the dominant mode of atmospheric variability (as defined through an EOF analysis) which resembles the observed SAM. We do not explore the dynamics of this atmospheric response here, but it is linked to a cooling of the lower stratosphere and a seasonal SAM-like

tropospheric anomaly. Instead, we focus on the transient response of the ocean and sea-ice to the atmospheric anomalies. But, first, let us describe analogous calculations carried out with the NCAR Community Climate model.

160 b. CCSM3.5

We use the Community Climate System Model version 3.5 (CCSM3.5) configured as in 161 Gent et al. (2010), Kirtman et al. (2012), Bitz and Polvani (2012), and Bryan et al. (2013). 162 All four studies describe the simulated climate of the CCSM3.5 and the latter two focus 163 on the Southern Ocean and Antarctic sea ice therein. The atmospheric component has a 164 finite-volume dynamical core and a horizontal resolution of $0.47^{\circ} \times 0.63^{\circ}$ with 26 vertical 165 levels. The horizontal grid of the land is the same as the atmosphere. The ocean and sea 166 ice have a resolution of nominally 1°. The ocean eddy parameterization employs the Gent 167 and McWilliams (GM) form (as in MITgcm), but with a GM coefficient varying in space 168 and time following Ferreira et al. (2005), as described in Danabasoglu and Marshall (2007). All of our integrations with CCSM3.5 have greenhouse gases and aerosols fixed at 1990s 170 level. The initial conditions were taken from a 1990s control simulation carried out with 171 the CCSM3. The CCSM3.5 was first run for 155 years (see Kirtman et al. 2012) with 172 ozone concentrations intended to be representative of 1990s levels that were prepared for 173 the CCSM3 1990s control integrations (see Kiehl et al. 1999). However, compared to more 174 recent estimates of ozone concentrations from the Atmospheric Chemistry and Climate and 175 Stratospheric Processes and their Role in Climate (AC&C/SPARC) dataset (Cionni et al. 176 2011), the CCSM3 estimates for 1990s resemble the level of ozone depletion in the Antarctic 177 stratosphere of approximately 1980, or about half the level of depletion since preindustrial 178 times. Hence, to create a quasi-equilibrated "high-ozone" control integration, with prein-179 dustrial ozone concentrations, we ran an integration where we first ramped up the ozone concentration for the first 20 years and then stabilized the ozone concentrations at 1960s 181 levels for another 50 years. We then ran an ensemble of 26 "abrupt low-ozone" integrations 182

by branching from the last 30 yrs of the high-ozone control. The magnitude of the prescribed ozone depletion is equal to the 2000s minus 1960s from the AC&C/SPARC dataset. Twenty of the ensemble members, with an annual cycle as in the MITgcm, were branched on September 1st and ran for 32 months, and six of the ensemble members were branched on January 1st and ran for 20 years.

As in the MITgcm, the atmospheric response a to ozone depletion in CCSM3.5 is a 188 positive SAM-like pattern with a maximum amplitude in Dec-Jan-Feb (Fig. 4). The pattern 189 is similar to that found in other models (see Thompson et al. 2011) albeit with stronger 190 zonal asymmetries, notably marked by a large trough centered on 90°W. At the peak of 191 the summer response, geopotential height anomalies at 500 mb are about ± 20 m, somewhat 192 weaker than those seen in the MITgcm. At the surface, however, sea level pressure anomalies 193 are typically ± 3 mb and are associated with surface wind anomalies of about 1 m s⁻¹ (see 194 Bitz and Polvani 2012), similar to those in the MITgcm. Given the differences between 195 the two coupled models, their surface responses to ozone depletion are remarkably similar 196 although the response in CCSM3.5 has larger zonal asymmetries. 197

In the zonal-mean, the wind stress responses of the two models are similar in shape and 198 magnitude although they are shifted relative to one another in latitudinal direction (Fig. 3). 199 For comparison, the surface wind stress pattern of the SAM in the NCEP-NCAR re-analysis 200 is also shown. The models responses fall on both sides of the location of the observed 201 SAM. These differences could reflect the differences in the representation of the ozone hole 202 in the two models as well as differences in their mean states and internal dynamics linking 203 the stratospheric cooling to the surface wind stress response. Son et al. (2010) found a 204 relationship between the tropospheric response to ozone depletion and the location of the 205 climatological jet in models participating to the CCMVal-2 inter-comparison project. 206

$_{\scriptscriptstyle{207}}$ 3. Ocean and Sea ice response in the MITgcm

208 a. The evolution of the transient SST response

Following the atmospheric response to ozone depletion, the ocean and sea ice cover adjust 209 to the changing winds (Fig. 5). The early (years 0-5) SST response consists of a zonally 210 symmetric dipole: a cooling between 50 and 70°S and a warming in the band 50-25°S 211 (there is also a weak cooling north of 25°S). This initial SST response is of significant 212 magnitude, typically ± 0.3 °C, and is similar to the SST signature of a positive SAM on 213 interannual timescales seen in observations and coupled GCMs (see, e.g. Watterson 2000; Hall and Visbeck 2002; Ciasto and Thompson 2008). It is primarily generated by anomalous 215 Ekman currents (see below). After two decades or so, the SST response changes noticeably 216 (Fig. 5, bottom left). The warm pole (50-30°S) has nearly doubled in magnitude while the 217 cold pole has weakened. 218

The ocean response is not limited to the surface (Fig. 5, right). Temperatures at 170 m exhibit a widespread warming south of 30°S with a peak around 40°S, with a slight cooling north of 30°S. The pattern of the subsurface response does not change over time but exhibits, as at the surface, a warming tendency at all latitudes south of 30°S. After 2 decades, the subsurface temperature peaks markedly at two latitudes, 40 and 60°S, where the anomalies reach up to 0.8°C, comparable in strength to the SST anomalies.

A continuous monitoring of the SST evolution over the first 40 years after the "ozone hole" inception shows that the initial dipole SST response (south of 25°S) slowly morphs into a warming (Fig. 6). By year 40, the character of the SST response more closely mirrors the subsurface temperature pattern than the early SST response. It is notable that the long term SST adjustment (30 years and longer) is similar to that found by Sigmond and Fyfe (2010) and Bitz and Polvani (2012) in response to ozone depletion. These previous studies did not present or discuss the time evolution of the ocean response. Sigmond and Fyfe (2010) carried out 100 year perturbation/control experiments and defined the response to ozone depletion

as the 100-y averaged difference between the perturbed and control runs. Bitz and Polvani (2012) carried out perturbation experiments in which the ozone hole was ramped up for 20 years and then maintained for an additional 30 years. They defined the response to ozone depletion as the difference between perturbed and control runs averaged over the last 30 years of integration. Clearly, in both cases, the responses were largely dominated by the long (multi-decadal) adjustments of the model ocean to ozone depletion.

Our results, however, suggest that there are two phases in the SST response: a fast response which has a dipole pattern, consistent with expectations from SAM/SST correlations
on interannual timescales, followed by a slow widespread warming of the SO similar to results
from previous GCMs studies. The transition between the two phases is seen after about 20
years in the MITgcm, when the initial cold SST response in the band 50-70°S transitions to
warming. SST variations in this band are particularly important because it coincides with
the region of seasonal sea ice fluctuations.

A closer look at the time evolution of the SST in the band 50-70°S is shown in Fig. 7.

The area-averaged SST falls by -0.3°C within a year and then slowly and almost linearly rises to cross zero around year 20. The SST increases for 200 years or so approaching a new equilibrium which is 1.5°C warmer than in the control run (not shown). Ozone depleting substances are no longer being emitted, so in the real world this forcing will not be present long enough for such a response to be realized. It is computed here to illustrate physical processes.

Despite the 20-member ensemble, significant noise remains in the ensemble mean areaaveraged SST due to internal variability. The grey shading and solid black line in Fig. 7
give a measure of the uncertainties in the time evolution of the SST¹. This suggests that the
fast SST response ranges between -0.1 and -0.4°C while the time of the sign reversal varies

1 They are computed as follows: 20x8 SST evolutions are constructed by combining the 20 short runs
(year 0-40) with the 8 long runs (year 41-350) and are fitted to a two timescale exponential form (see Eq.

253

254

255

256

⁽year 0-40) with the 8 long runs (year 41-350) and are fitted to a two timescale exponential form (see Eq. 8 below). The solid black line is the mean of these 160 evolutions while the grey shading indicates plus or minus one standard deviation

between 15 and 30 years.

In concert with SST changes around 70-50°S, sea ice cover also significantly evolves in response to ozone depletion (Fig. 8). As expected, sea ice expands in the presence of colder SSTs and retreats when SSTs become positive, after about 20 years. This increase is seen in all seasons but is largest in winter when sea ice extent is at its peak. Note that the cold SST response is largest in summer when the atmospheric perturbations is the strongest but persists throughout the year (see Fig. 6). The sea ice perturbations are small but significant, representing typically a few % of the climatological seasonal change.

265 b. Role of interior ocean circulation in SST evolution

We now address the mechanisms that drive the evolution of the SST response. We first focus on the MITgcm and go on to see whether similar mechanisms are at work in CCSM3.5.

1) The fast response

On short (~year) timescales the ocean response is essentially confined to the mixed 269 layer. The SST dipole is primarily forced by Ekman current anomalies due to the SAM-like 270 surface wind response (Fig. 5). South of 45°S, increased surface westerly winds result in 271 an anomalous northward Ekman flow which advects cold water from the South. North of 45°S, the opposite happens. The SST tendency due to this forcing, $v'\partial_y \overline{T}$, is plotted in Fig. 9 (dashed-dotted) along with the SST response (red, both averaged over year 2-5). 274 Here, $\partial \overline{T}/\partial y$ is taken from the control, while the full anomalous Eulerian currents v', not 275 just its Ekman component, are used in the computation. For convenience, the tendency is 276 expressed in W m⁻² taking a sea water density ρ_o of 1030 kg m⁻³, a water heat capacity C_p 277 of 3996 J kg⁻¹ K⁻¹, and a constant mixed layer depth h_s of 30 m (the thickness of the top 278 model level). The pattern of anomalous advection tendency closely matches that of the SST 279 dipole and is of the correct magnitude to explain the SST response (except north of 25°S 280

where vertical advection is an important forcing, see below).

In contrast, the net air-sea flux anomaly F' (dominated by the latent contribution, positive downward) damps the SST anomaly to the atmosphere (Fig. 9, solid black). Net air-sea heat fluxes and horizontal advection term (dashed-dotted) closely oppose one another over the first few years. The initial SST dipole is thus the quasi-equilibrium response to the fast mixed layer dynamics:

$$\frac{\partial T'}{\partial t} \simeq -v'\partial_y \overline{T} + F'_a - \lambda T' \simeq 0. \tag{1}$$

where the net air-sea heat flux anomaly F' is made up of two contributions: a term F'_a 287 driven by changes in the atmospheric state (independent of SST anomalies, e.g. surface 288 wind changes, shortwave changes) and a SST damping term that varies linearly with T' on 289 a timescale λ^{-1} (positive λ implies a damping to the atmosphere). The fast SST response 290 to ozone depletion in the MITgcm is similar to the SST anomaly associated with a positive 291 phase of the SAM, in observations and models alike (Ciasto and Thompson 2008; Sen Gupta 292 and England 2006). Because our set-up is strongly zonally symmetric, the SST forcing is 293 largely dominated by meridional Ekman advection. Note, however, that in more realistic configurations air-sea fluxes due to zonal asymmetries of the SAM pattern may be important locally (Ciasto and Thompson 2008; Sallée et al. 2010). 296

297 c. The slow response

The Ekman current anomalies are divergent and drive anomalous upwelling south of 50°S and north of 35°S and an anomalous downwelling between these two latitudes. The Eulerian MOC response consists then of two cells closely matching the surface wind stress anomalies (Fig. 10). South of 35°S where there are no meridional boundaries, the Eulerian MOC streamlines are vertical in the interior (as expected in the geostrophic limit) with return flows in the top and bottom Ekman layers. North of 35°S, meridional barriers allow for a mid-depth geostrophic return flow. At all latitudes, however, the strength of the Eulerian

MOC just below the Ekman layer is very well approximated by the theoretical prediction $\tau_x/(\rho_o f)$ (on monthly and longer timescales) where τ_x is the zonal mean zonal wind stress and f the Coriolis parameter (not shown).

Anomalies of the residual-mean circulation (sum of the Eulerian and parameterized eddy-308 induced circulations) are plotted in Fig. 11. Comparison of Figs. 11b and 10 (same averaging 309 periods) shows that the residual-mean MOC anomalies are dominated by the Eulerian flow, retaining a clear connection to the pattern of surface wind anomalies. However, in analogy with the mean state balance, the eddy-induced MOC anomalies tend to oppose the 312 wind-driven circulation anomalies, particularly south of 35°S where there are no meridional barriers. As a result, the residual-mean MOC anomalies are weaker than the wind-driven 314 Eulerian MOC anomalies by as much as a factor two. On average over the band 70-50°S, 315 the residual-mean upwelling response is about 1 m year⁻¹, compared to 1.5 m year⁻¹ for the 316 Eulerian component (Fig. 12, top left). Note that the cancellation of the Eulerian vertical 317 velocity by the eddy-induced component is similar at all depths. 318

Because ocean temperature increases upward north of 55°S (see color contoured in Fig. 319 10, middle), the downwelling and upwelling at these latitudes are expected to result in 320 warming and cooling, respectively. However, the near-surface temperature stratification 321 south of 55°S is reversed, with warmer water at depth because of the presence of seasonal 322 sea ice (Fig. 10, bottom). Then, upwelling south of this limit results in a warming. This 323 is indeed observed in subsurface layers as shown in Fig. 11. Meridionaly, the maximum temperature responses are clearly associated with branches of upwelling/downwelling. In 325 the vertical, the temperature response peaks just below the mixed layer, around 100-200 m, 326 where the summertime vertical stratification $\partial \overline{T}/\partial z$ is the largest. This is within reach 327 of the wintertime deepening of the mixed layer which, on average in the band 70-50°S, 328 extends to about 150 m at its deepest. The cold SST response between 70 and 50°S stands 329 out over years 1-5, when subsurface temperature anomalies remain weak (Fig. 11a). As 330 time increases, however, the subsurface temperature anomalies grow larger and larger and 331

eventually imprint themselves into the surface layer, through entrainment, so that by years
21-25, the cold SST anomaly has disappeared.

As shown in Fig. 11d, the time evolution of the subsurface (170 m deep) temperature response around 60°S is nearly linear over the first 40 years. A best fit gives an average warming rate of 0.017 °C year⁻¹ (dashed black). This values is readily explained by the annual mean residual upwelling anomaly w_{res} (\sim 1 m year⁻¹) acting on the mean temperature stratification $\partial \overline{T}/\partial z$ (\sim 0.019 °C m⁻¹) at this location. This confirms that the subsurface temperature response is well approximated by:

$$\frac{\partial T'_{sub}}{\partial t} \simeq -w'_{res} \frac{\partial \overline{T}}{\partial z}.$$
 (2)

How much time is required for the upwelling of warm waters to compensate the initial cold SST response around 60°S? The fast SST response at 60°S peaks at about -0.4°C (year 3, see Fig.6). Assuming that subsurface temperatures are efficiently carried into the mixed layer through entrainment, the initial SST response would be cancelled when the subsurface temperature perturbation reaches +0.4°C. This takes about 20-25 years (Fig. 11d), in good agreement with the SST evolution shown in Fig. 6.

After a couple of decades (Fig. 11c), the ocean has warmed south of 30°S at all depths (due to upwelling/downwelling collocated with positive and negative temperature stratification) and cooled north of 30°S (due to upwelling of cold water). This distribution resembles 348 the averaged responses found by Sigmond and Fyfe (2010) and Bitz and Polvani (2012). The latter study identifies upwelling/downwelling anomalies driven by the SAM-like atmo-350 spheric perturbation as a primary driver of the temperature response. In addition, Bitz and 351 Polyani (2012) shows (see their Fig. 3) that this effect is at work both at coarse (1°) and 352 eddy-resolving (0.1°) resolutions in CCSM3.5. Although the relative importance of eddies 353 and mean flow vertical advection depends on resolution, their result suggests that ocean 354 eddies do not have a major influence on the quasi-equilibrium response. Note, however, this 355 does not imply that eddies do not have an influence on the rate at which quasi-equilibirum 356 response is approached (see below). 357

Two aspects of the temperature evolution deserve comment:

358

1) The fast SST response is driven primarily by anomalous horizontal rather than vertical advection. A scaling of these two terms is:

$$\alpha = \frac{v'_{res}\overline{T}_y}{w'_{res}\overline{T}_z} \sim \frac{\overline{T}_y}{\overline{T}_z} \frac{L_y}{h_s},\tag{3}$$

where \overline{T}_y is the meridional temperature gradient at the surface, \overline{T}_z the stratification just below the mixed layer, L_y the width of the upwelling zone ($\sim 20^{\circ}$ for the band 50-70°S). We assume that, at the scaling level, $v'_{ek}/w'_{ek} \sim v'_{res}/w'_{res}$. We find that α is about 15-363 30 (for $\overline{T}_z = -0.015$ -0.020 °C m⁻¹, $\overline{T}_y = 4$ -6×10⁻⁶ °C m⁻¹, and $h_s = 30$ m). It is large 364 because the width of the upwelling zone is much greater than the depth of the horizontal 365 flow $(L_y \gg h_s)$ or equivalently, through volume conservation, $|v'_{ek}| \gg |w'_{ek}|$). Despite the 366 fact that $\overline{T}_z \gg \overline{T}_y$, horizontal advection dominates. In subsurface layers, by contrast, there 367 are no air-sea fluxes and little damping. Then, subsurface temperature anomalies induced 368 by anomalous upwelling grow unabated over decades and are eventually imprinted into the 369 surface layers through entrainment during the fall/winter deepening of the mixed layer. 370

2) The impact of (parameterized) eddies is significant in setting the subsurface warming 371 rates. As shown above the residual-mean overturning anomalies are dominated by the Eulerian wind-driven component on yearly averages but is partially compensated by eddy-induced 373 MOC anomalies. The anomalous Eulerian component is much larger than the annual mean 374 during summer months when the anomalous surface wind stress peaks, but is vanishingly 375 small in winter. By contrast, the eddy-induced circulation anomalies, which are proportional 376 to the perturbations in isopycnal slope, are more steady. This is reflected in the yearly fluc-377 tuations superimposed on the slow increase of the subsurface temperature anomalies at 60°S 378 shown in Fig. 11d. During summer, the wind forcing dominates and isotherms are lifted. 379 During wintertime, the wind forcing disappears and only the eddy-induced MOC persists: 380 isotherms are relaxed back toward their unperturbed position. In the annual mean, the 381 Eulerian vertical advection dominates, but the rate of temperature increase in subsurface 382 layers is significantly affected by the eddy contribution. If the wind forcing was the only 383

process acting, the rate of anomalous upwelling at 60°S would be 2 m year⁻¹, twice as fast as the rate due to the anomalous residual flow (1 m year⁻¹). Thus, the upwelling anomaly w'_{res} in Eq. (2) can be expressed as:

$$w'_{res} = \delta w'_{ek} = \delta \frac{\partial}{\partial y} \left(\frac{\tau'_x}{\rho_o f} \right) \tag{4}$$

where δ is an "eddy compensation" parameter which ranges from 1 (no eddy compensation) 387 to 0 (exact eddy compensation). In the MITgcm experiments, δ =0.3-0.5 in the band on 388 upwelling (70-50°S) at 100-200 m depth. It is interesting that in the mean (i.e. control state) 389 Eulerian and eddy-induced MOC also compensate roughly by this amount (see Marshall and Radko 2003). 391 In summary, we find that the warming of SST on long timescales in the band 70-50°S is 392 due to upwelling of warm water (primarily driven by Ekman divergence). The time to the 393 SST reversal is well approximated by the time necessary for the subsurface warming to offset 394 the initial cold SST response, about 20 years here. The long term temperature response is 395 consistent with previous findings and accounts for the retreat of sea ice in response to ozone 396 depletion on long (multidecadal) timescales. 397

4. Ocean and Sea Ice Response in CCSM3.5

399 a. Temperature and sea ice response

The response to ozone depletion in CCSM3.5 has many similarities with that found in the MITgcm, but also some important differences of detail. Of most significance is that the SST response again has two phases: first a dipole response in the meridional direction followed by a widespread warming of the Southern Ocean, as in the MITgcm (Figs. 13 and 14). CCSM3.5 has much more realistic geometry than the MITgcm configuration and so the initial SST response exhibits important zonal asymmetries, unlike the MITgcm (Fig. 13, top). In particular, the cold SST pole around 60°S is interrupted downstream of the

Drake Passage where the warm pole extends across the ACC into the Western part of the
Weddel Sea. This feature is also found in the observed SST response to a positive phase of
the SAM (see Ciasto and Thompson 2008) and corresponds to a region where air-sea heat
fluxes, rather than Ekman currents, dominate the SST anomaly forcing. Note, however, that
the SST response to ozone depletion in CCSM3.5 differs from the observed SAM-forced SST
anomaly in some other aspects. For example the negative pole in the Pacific sector is larger
and extends further equatorward.

As in the MITgcm experiment, over time the SST (and subsurface) responses morph into a widespread warming (Fig. 13, bottom). The transition between the two phases however occurs much faster in CCSM3.5, after only 3-5 years (Fig. 14). Around 60°S, between years and 5, cold SST anomalies during summer (at the peak of the wind forcing) alternate with warm anomalies during winter. At 70°S, the cold SST response reappears during most summers for nearly 2 decades.

The amplitude of the SST response in CCSM3.5 is weaker than in the MITgcm, with peak 420 values of ± 0.3 °C (compared to ± 0.6 °C in MITgcm), reflecting the difference in the surface 421 wind response to ozone depletion in the two models. Largely due to the zonal asymmetries of 422 the SST response in CCSM3.5, the zonal mean initial response is only -0.2°C (Fig. 14) and 423 averaged between 70 and 50°S it is only -0.05°C (Fig. 7, right, red solid). For a meaningful 424 comparison with the MITgcm therefore, the SST evolution averaged over the area comprising 425 the initial cold pole (see Fig. 13, top) is also shown in Fig. 7 (right, dashed red). According to this measure, the initial SST response is larger (-0.15°C) in magnitude and changes sign 427 at a later time (5 yr) than in the zonal average. When comparing the two models, the 428 initial cooling response in CCSM3.5 is also partially obscured by the warming trend which 429 grows much more rapidly than in the MITgcm (see below). Despite these differences, the 430 two phases of the SST response are clearly evident in Fig. 7 (left). After the sign reversal 431 during year 3-5, the SST continues to increase for a few years more and appears to stabilize 432 around 0.15°C after a decade or so. Note that only 6 ensemble member are available after 433

3 years and so larger variability is evident. The appearance of a stationary state after 10 years may not be a robust feature.

The rapid transition between the two phases is also evident in the sea ice response. The
sea ice area only increases during the first winter following the ozone hole inception (Fig.
8, right) while the summer sea-ice area decreases sharply. The area of winter sea-ice also
eventually declines. The magnitude of the sea-ice area decline in the slow phase of the two
models is similar although the decline occurs about a decade sooner in CCSM3.5.

441 b. Role of ocean circulation on temperature evolution

The underlying dynamics of the SST evolution in CCSM3.5 is similar that in the MITgcm 442 although the magnitudes of key terms in the heat budget and implied timescales are different. 443 In the zonal mean, the initial dipole SST anomaly is largely explained by the anomalous 444 Ekman response (Fig. 9, right). To match the short-lived initial response, the forcing terms 445 and SST anomalies in Fig. 9 (right) are averaged over 2 years. The Ekman forcing term (and the SST response) are about half those found in the MITgcm. The air-sea flux anomalies act 447 to damp the SST response at all latitudes. The air-sea flux anomalies and Ekman forcing 448 again tend to balance each other. There is one noticeable exception between 60 and 50°S 449 where the air-sea flux term is larger in magnitude than the Ekman term. Here, the air-sea 450 flux warms the surface faster than it is cooled by Ekman advection. More detailed analysis 451 reveals that this is due to an increased shortwave absorption at the surface due to a decrease 452 of the cloud fraction (not shown). 453

The other important mechanism identified in the MITgcm experiment is the wind-driven subsurface warming below the initial cold SST anomaly. Fig. 12 (right) shows the vertical velocity anomalies and the resulting tendency $-w'_{res}\frac{\partial \overline{T}}{\partial z}$ in CCSM3.5 (at two depths where the values are largest). South of 60°S, the anomalous Ekman divergence drives upwelling in a region where the temperature decreases toward the surface (Fig. 12, top right). As in the MITgcm, this results in a positive tendency. Note that w'_{res} is larger at 70 than at 130 m depth, but that the temperature tendency at 70 m is much smaller because this level lies within the mixed-layer and the temperature stratification is weak. North of 60°S, the mixed layer is shallower and strong tendencies are found closer to the surface. The large positive tendency, of 0.1°C year⁻¹, centered on 50°S is due to downwelling of warm waters while the large negative tendency around 40°S is due to upwelling of cold water.

The vertical advection tendencies in CCSM3.5 are significantly larger than in the MITgcm (Fig. 12, bottom, note the different vertical scales in the two panels), typically by a factor 2 in the band 70-50°S (see also estimated values in Table 1 and section 5 below).

Comparing the annual- and zonal-mean wind stress responses in the MITgcm and CCSM3.5 468 (Fig. 3), it appears that 1) the responses of the two models are shifted in the meridional di-469 rection, one with respect to the other (surface wind anomaly peaks around 65°S in CCSM3.5 470 but around 55°S in the MITgcm) and 2) the meridional scale of the wind change in CCSM3.5 471 is smaller than in the MITgcm. This leads to stronger wind curl anomalies and hence larger 472 Eulerian upwelling rates. In addition, the cancellation of the wind driven upwelling by the 473 eddy-induced vertical velocity differs between the two models. In contrast with the MITgcm 474 (Fig. 12, top left), eddy-induced contributions to upwelling rates are very small compared 475 to the Eulerian mean down to 100 m depth in CCSM3.5. The combination of a larger 476 wind-driven upwelling and a weaker eddy cancellation largely explains the stronger warming 477 tendencies seen in CCSM3.5 (Fig. 12, bottom), and as we shall see, is a major factor in the 478 shorter cross-over time from cooling to warming.

5. Discussion and development of a simplified model

The discussion in sections 3 and 4 have enabled us to identify common robust mechanisms of warming and cooling in the two models. Here we use the insights gained to present a simplified model of the response of the ocean to SAM forcing which exposes those processes in a transparent way.

a. Formulation

To aid our discussion, motivated by diagnostics of our two coupled models, we present the following simple model of the temperature response:

$$\frac{\partial T'}{\partial t} = -v'_{res} \frac{\partial \overline{T}}{\partial y} + F'_a - \lambda T' + \Lambda_e T'_{sub}$$
 (5)

$$\frac{\partial T'_{sub}}{\partial t} = -w'_{res} \frac{\partial \overline{T}_{sub}}{\partial z} - \lambda_{sub} T'_{sub}$$
 (6)

where T' is the SST response, T'_{sub} the subsurface temperature response (imagined to be typical of the seasonal thermocline) and Λ_e represents the entrainment timescale of the 489 subsurface temperature into the mixed layer. The subsurface temperature is assumed to adjust on a timescale λ_{sub}^{-1} which encapsulates complex dynamics relevant to the equilib-491 rium response and adjustment of the SO seasonal thermocline. The overbar denotes the 492 climatological state of the control run, and the prime is the perturbation in response to 493 the anomalous wind forcing. In the absence of a dynamical response in the ocean interior 494 $(w'_{res} \simeq 0)$ and/or of an influence of the interior onx the surface layer $(\Lambda_e = 0)$, the SST 495 anomaly equation reduces to: 496

$$\frac{\partial T'}{\partial t} = \tilde{F} - \lambda T' \tag{7}$$

where $\tilde{F} = F'_a - v'_{res}\partial_y \overline{T}$ is the atmospheric forcing of the mixed layer by air-sea flux and Ekman current anomalies. This is the classical model of midlatitude SST variability (Frankignoul and Hasselmann 1977).

We are interested in the response to a step-function wind change. Assuming a constant atmospheric forcing $(v'_{res}, w'_{res}, F'_a = \text{const})$ for t > 0, solutions are given by:

$$T' \simeq \frac{\tilde{F}}{\lambda}(1 - e^{-\lambda t}) + \frac{\Lambda_e}{\lambda}T'_{sub}$$
 (8)

$$T'_{sub} = \frac{-w'_{res}\partial_z \overline{T}_{sub}}{\lambda_{sub}} (1 - e^{-\lambda_{sub}t}) \tag{9}$$

in the limit $\lambda_{sub} \ll \lambda$ appropriate to our models. The subsurface temperature (9) grows monotonically on a timescale λ_{sub}^{-1} . The SST response (8) is the sum of two exponential

functions: one captures the fast response driven by mixed-layer dynamics while the second 504 one, $\Lambda_e/\lambda \times T'_{sub}$, is driven by the slow ocean interior dynamics. Note that for $t \ll \lambda_{sub}$, T'_{sub} 505 increases linearly at a rate given by $-w'_{res}\partial_z\overline{T}_{sub}t$ as found in the coupled GCMs. Parameters 506 obtained from a best fit of Eqs. (8) and (9) to the SST and subsurface temperature evolution 507 in both the MITgcm and CCSM3.5 are given in Table 1. The best-fit curves are shown in 508 Fig. 15 (solid) with their fast and slow components (dashed). It is important to emphasize that the response to a step function in the classical model (7) reduces to the fast component 510 if the ocean is passive (lower dashed curves in Fig. 15). Thus both coupled GCMs depart 511 significantly from the Frankignoul and Hasselmann (1977) classical model, attesting to the 512 active role of ocean circulation in modulating the SST response. 513

The fitted parameters in Table 1 are clearly estimates and depend on the underlying assumptions of the simple model Eqs. (5) and (6). They nonetheless provide useful insights in to processes at work and the differences between the two GCMs. There are two key differences between the coupled models which we now discuss in turn: air-sea fluxes/damping rates and the response of the interior ocean.

519 b. Air-sea interactions

The first difference that stands out is in the strength of the air-sea heat exchanges. The 520 atmospheric-driven forcing \tilde{F}_F (= $\rho_o C_p h_s \tilde{F}$ in W m⁻²) is -0.7 W m⁻² in the MITgcm and 521 $-1.1~\mathrm{W}~\mathrm{m}^{-2}$ in CCSM3.5 (average values in the band 70-50°S). Comparison with Fig. 9 522 suggests that \tilde{F}_F largely comprises the anomalous Ekman advection in the MITgcm, but is 523 significantly amplified by F'_a in CCSM3.5 (possibly because of the larger zonal asymmetries 524 in CCSM3.5). Changes in the atmospheric circulation (a positive SAM here) and ozone 525 concentration are both expected to affect the radiation reaching the surface. Recently, Grise et al. (2013) showed that ozone depletion could alter the top-of-the-atmosphere longwave and shortwave fluxes by a few W m⁻² in the band 70-40°S through a modulation of the 528 cloud fraction. A similar impact on the surface fluxes is anticipated (regardless of the 529

ocean response) although we cannot discriminate between the MITgcm and CCSM3.5 in 530 this respect. In addition, the estimated heat flux feedback $\lambda_F = \lambda/(\rho_o C_p h_s)$ is much larger 531 in CCSM3.5 than in the MITgcm (6.7 and 1.5 W m⁻² K⁻¹ respectively). We do not have 532 good estimates of the heat flux feedback in the Southern Ocean. Frankignoul et al. (2004) find 533 that λ_F is typically about 15-20 W m⁻² K⁻¹ at the local scale in the mid-latitudes but tends 534 to decrease significantly at the basin scale ($\sim 10~\mathrm{W}~\mathrm{m}^{-2}~\mathrm{K}^{-1}$) in the North Atlantic/Pacific. It is expected to decrease further at the global scale of the SO. Again, zonal asymmetries in CCSM3.5 probably contribute to the difference between the two models, enhancing air-sea 537 contrast and damping rates as air parcels move above the Southern Ocean. Cloud and sea ice feedbacks are also likely contributors. Despite the factor of 4 difference between the 539 CCSM3.5 and MITgcm heat flux feedback, neither can be ruled out as unrealistic. Thus, 540 it appears that the air-sea heat interactions (forcing and damping) are significantly more 541 intense in CCSM3.5 than in the MITgcm. 542

543 c. Response of the interior ocean

The Frankignoul and Hasselmann (1977) model is modified by ocean interior dynamics in our simple model. In the limit $t \ll \lambda_{sub}^{-1}$, the SST response (8) becomes:

$$T' \simeq \frac{\tilde{F}}{\lambda} (1 - e^{-\lambda t}) - \frac{\Lambda_e}{\lambda} w'_{res} \partial_z \overline{T}_{sub} t.$$
 (10)

The time t_r at which the SST changes sign, $T'(t_r) = 0$, then depends on λ but no longer on λ_{sub} . Further assuming $\lambda^{-1} \ll t \ll \lambda_{sub}^{-1}$, t_r simplifies to:

$$t_r \simeq \frac{1}{\Lambda_e} \frac{-\tilde{F}}{-w'_{res}\partial_z \overline{T}_{sub}} = \frac{1}{\Lambda_e} \frac{v'_{res}\partial_y \overline{T} - F'_a}{-w'_{res}\partial_z \overline{T}_{sub}}$$
(11)

Note that the above expression does not apply well to the CCSM3.5 case where t_r is only a factor 2 smaller than λ_{sub} . Nonetheless, Eq. (11) points to the key role of residual circulation in driving the change of sign. The larger v'_{res} the longer the transition (through a larger initial cooling of SST) while the larger w'_{res} the shorter the transition (through increases

of the subsurface warming rate). As pointed out in Eq. (4) (and Fig. 12), the residual 552 upwelling flow results from a cancellation (by a factor δ) of the wind-driven upwelling by 553 the (parameterized) eddy-induced downwelling. However, the cancellation of the Ekman 554 horizontal flow by the eddy-induced circulation is relatively weak in comparison with that 555 of the vertical flow. This is because the Eulerian and eddy-induced streamfunctions do not 556 have the same vertical distribution. The Eulerian streamfunction is constant over the fluid column and decays to zero at the surface within the Ekman layer (~ 30 m), i.e. the horizontal flow is very confined vertically (Fig. 10). In contrast, the eddy induced flow near the surface 559 is spread over a deeper layer, of about 200 m. This mismatch between the vertical scales of 560 the two MOC components is observed in eddy-resolving simulations (see Abernathey et al. 561 2011; Morrison and Hogg 2013) and should not be considered an erroneous effect of the Gent 562 and McWilliams eddy parameterization employed in the coupled GCMs (although the use of 563 a tapering scheme in the GM scheme may have an influence). This suggests that $w'_{res} = \delta w'_{ek}$ 564 and $v'_{res} \simeq v'_{ek}$ is a better choice in which case: 565

$$t_r \simeq \frac{1}{\Lambda_e} \frac{v'_{ek} \partial_y \overline{T} - F'_a}{-\delta w'_{ek} \partial_z \overline{T}_{sub}}$$
 (12)

In the limit of perfect eddy compensation ($\delta = 0$), t_r would go to infinity as there would be no subsurface upwelling and warming and the initial cold SST response would persist indefinitely. In the limit of no eddy compensation ($\delta=1$), the transition t_r would be more rapid. Eq. (12) emphasizes that the eddy processes (vertical structure, magnitude) may be key in determining the timescale of the SST reversal.

Finally, we point to the role of the entrainment time scale Λ_e^{-1} which modulates the imprint of the subsurface temperature onto the SST. It is shorter in CCSM3.5 than in the MITgcm, 0.4 and 1.5 yr, respectively (Table 1). The shorter CCSM3.5 timescale (promoting a shorter transition time t_r) could possibly be due to the shallower depth of the peak subsurface tendencies (see Fig. 12) or the use of a mixed layer scheme and higher vertical resolution. In both models however, the ratio λ/Λ_e which appears in Eq. (8), is about 0.6 and the warming trend of the SST mimics that of the subsurface temperature (Fig. 15).

6. Conclusion

In this study, we have explored the ocean and sea ice response to ozone depletion in two coupled GCMs. The ozone depletion is imposed as a step function and we compute the transient response of the coupled system to this perturbation. As in other studies, the surface westerly winds shift poleward and strengthen during summer in response to ozone depletion; this atmospheric response is similar to the positive phase of the SAM.

The first key result of our study is that the SST response to this wind perturbation in 584 the Southern Ocean has two phases (see Fig. 1 for a schematic). The fast response occurs on 585 monthly timescale following the SAM-like wind perturbation, but also builds up over a few 586 years. It is mediated by mixed layer dynamics and air-sea interaction. It consists of a dipole, 587 with a cooling south of the ACC (where the surface wind increases) and a warming where 588 surface westerly winds weaken (around 35°S) (Fig. 1, left). This response is primarily driven 589 by anomalous Ekman advection with air-sea heat interactions acting as a damping. The slow 590 response is due to interior ocean dynamics. The northward Ekman flow at 70-50°S drives 591 upwelling south of the ACC which brings warm water to the surface. At these latitudes 592 where sea ice expands seasonally, the water column is stratified by salinity and cold water 593 at the surface lies over warm water below. On long (multi-year) time scales, this warmth 594 can be entrained into the mixed layer and counteracts the initial SST cooling (Fig. 1, right). 595 Eventually, the SST response to ozone depletion is a widespread warming of the SO. 596

The second key result of our study is that there is no inconsistency between inferences based on SAM/SST correlations and modeling studies of the SO response to ozone depletion. Sigmond and Fyfe (2010) and Bitz and Polvani (2012) found that ozone depletion drives a warming of the SO and sea ice loss in coupled GCMs. The SST/sea ice signatures of the positive phase of the SAM, however, suggest that ozone depletion through its surface wind impact should generate a SST cooling around Antarctica and a sea ice expansion (Goosse et al. 2009). These two conclusions are reconciled within one framework by our results showing a two-timescale response to ozone depletion.

Finally, a related overall outcome is that ozone depletion could drive a transient expansion of the sea ice cover around Antarctica that could have contributed to the observed sea ice expansion of the last 3 decades (Parkinson and Cavalieri 2012). In both GCMs used here, the initial sea ice response to an abrupt ozone depletion is one of expansion, followed by a contraction of the sea ice cover as the surface warms. This long term response is consistent with findings by Sigmond and Fyfe (2010) and Bitz and Polvani (2012)). However, the true (time-varying) influence of ozone depletion on the sea ice extent will critically depend on the timescale of the transition from cooling to warming.

An important corollary of this study is that analysis of the relationship between sea ice 613 cover and SAM changes in observations may require more sophisticated tools than previ-614 ously used in the literature (e.g. simultaneous correlations or trends). In a recent study, 615 for example, Simpkins et al. (2012) computed the sea ice cover trends that are linearly con-616 gruent with the SAM during summer. To do this, they regressed sea ice anomalies onto 617 the detrended SAM index, and then multiplied the resulting regression coefficients by the 618 trend in the SAM. Such an approach effectively assumes that there is a single relationship 619 between SAM and sea ice cover changes that applies on all times scales, or, equivalently that 620 there is only one (fast) timescale response. Simpkins et al. (2012) (and others, see references 621 therein) found, using such congruency analysis, that the SAM trends explain less 15% of the 622 observed sea ice trends. This is not surprising in the light of our results: we do not expect 623 that the simultaneous (3-month averaged) relationship between SAM and sea ice cover would capture their relationship on long multidecadal trends. Therefore, we argue that such low 625 congruency obtained in observations does not rule out a dynamical link between SAM and 626 sea ice trends of the past 3 decades. A more accurate exploration of the SAM-sea ice link 627 needs to account for the two-timescale response. 628

Although the two-timescale SST response is a robust result seen in the two GCMs studied here and the mechanisms of this response are largely similar in the two GCMs, the timescale of the transition between the cold and warm SST phases around Antarctica is poorly constrained, being 20 years in the MITgcm and 3-5 years in CCSM3.5.

Two main sources of uncertainties have been identified: the nature of the air-sea in-633 teraction and the response of the interior ocean. Air-sea heat fluxes are partly driven by 634 atmospheric changes (notably changes in wind and cloud effects) and partly by rates of 635 damping of the SST anomaly once it is created. Parameterized mesoscales eddies control 636 the effective rate of subsurface warming by partially canceling the wind-driven upwelling. We emphasize that in both GCMs, eddy processes are parameterized. Eddy-resolving simulations have shown that such cancellation is difficult to capture in parameterization schemes 639 (e.g. Hallberg and Gnanadesikan 2006; Abernathey et al. 2011). More studies are required to better quantify these processes, to constrain the transition timescale using coupled GCMs, 641 process studies and observations. 642

Despite the above caveats, our results robustly demonstrate that the Southern Ocean responds to wind on multiple timescales, reconciling previously contradicting views. Importantly, regardless of the true timescale of transition between the fast and slow phases, our results highlight the need to revise the classical model of extratropical air-sea interactions for the Southern ocean to account for the interior ocean dynamics.

Acknowledgments.

DF was supported in part by a NASA MAP grant. JM, SS and AP obtained partial support from a NSF FESD project on the impact of the ozone hole on the Southern Hemi-sphere climate. Funding for CB was provided by the National Science Foundation (NSF PLR-1341497).

APPENDIX

654

655

653

The MITgcm

All components use the same cubed-sphere grid at a low resolution C24, yielding a resolution of 3.75° at the equator (Adcroft et al. 2004). The cubed-sphere grid avoids problems associated with the converging meridian at the poles and ensures that the model dynamics at the poles are treated with as much fidelity as elsewhere.

The atmospheric physics is of 'intermediate' complexity, based on the "SPEEDY" scheme

(Molteni 2003) at low vertical resolution (5 levels, one in the stratosphere, three in the troposphere and one in the boundary layer). Briefly, it comprises a 4-band radiation scheme, a
parametrization of moist convection, diagnostic clouds and a boundary layer scheme. The 3km deep, flat-bottomed ocean model has 15 vertical levels, increasing from 30 m at the surface
to 400 m at depth. The background vertical diffusion is uniform and set to 3×10^{-5} m² s⁻¹.

The sea-ice model is based on Winton (2000)'s two and a half layer thermodynamic
model with prognostic ice fraction, snow and ice thickness (employing an energy conserving

formulation). The land model is a simple 2-layer model with prognostic temperature, liquid ground water, and snow height. There is no continental ice. The seasonal cycle is represented (with a 23.5° obliquity and zero eccentricity) but there is no diurnal cycle.

Finally, as discussed by Campin et al. (2008), the present coupled ocean-sea ice-atmosphere model achieves perfect (machine-accuracy) conservation of freshwater, heat and salt during extended climate simulation. This is made possible by the use of the rescaled height coordinate z^* (Adcroft and Campin 2004) which allows for a realistic treatment of the sea ice-ocean interface. This property is crucial to the fidelity and integrity of the coupled system. The set-up is identical to that used in Ferreira et al. (2010, 2011) and very similar to that of Marshall et al. (2007) and Enderton and Marshall (2009) (see Ferreira et al. (2010) for key

differences).

679

680

REFERENCES

- Abernathey, R., J. Marshall, and D. Ferreira, 2011: The dependence of southern ocean meridional overturning on wind stress. *J. Phys. Oceanogr.*, 41, 2261–2278.
- Adcroft, A., J. Campin, C. Hill, and J. Marshall, 2004: Implementation of an atmosphere-
- ocean general circulation model on the expanded spherical cube. Mon. Wea. Rev., 132,
- 685 2845-2863.
- Adcroft, A. and J.-M. Campin, 2004: Re-scaled height coordinates for accurate representation of free-surface flows in ocean circulation models. *Ocean Modell.*, **7**, 269–284.
- Bitz, C. M. and L. M. Polvani, 2012: Antarctic climate response to stratospheric ozone depletion in a fine resolution ocean climate model. *Geophys. Res. Lett.*, **39**, L20 705.
- Bryan, F. O., P. R. Gent, and R. Tomas, 2013: Can southern ocean eddy effects be parameterized in climate models? *J. Climate*, submitted.
- Campin, J.-M., J. Marshall, and D. Ferreira, 2008: Sea ice-ocean coupling using a rescaled vertical coordinate z^* . Ocean Modell., 24, 1–14.
- Ciasto, L. M. and D. W. J. Thompson, 2008: Observations of large-scale ocean—atmosphere interaction in the southern hemisphere. *J. Climate*, **21**, 1244–1259.
- Cionni, I., et al., 2011: Ozone database in support of CMIP5 simulations: Results and
 corresponding radiative forcing. Atmos. Chem. Phys. Discuss., 11, 10875–10933.
- Comiso, J. C. and F. Nushio, 2008: Trends in the sea ice cover using enhanced and compatible amsr-e, ssm/i, and smmr data. *J. Geophys. Res.*, **113**, C02S07.

- Danabasoglu, G. and J. Marshall, 2007: Effects of vertical variations of thickness diffusivity in an ocean general circulation model. *Ocean Modell.*, **18**, 122–141.
- Enderton, D. and J. Marshall, 2009: Explorations of atmosphere-ocean-ice climates on an aqua-planet and their meridional energy transports. *J. Atmos. Sci.*, **66**, 1593–1611.
- Ferreira, D., J. Marshall, and J.-M. Campin, 2010: Localization of deep water formation:
- role of atmospheric moisture transport and geometrical constraints on ocean circulation.
- J. Climate, **23**, 1456–1476.
- Ferreira, D., J. Marshall, and P. Heimbach, 2005: Estimating eddy stresses by fitting dy-
- namics to observations using a residual mean ocean circulation model and its adjoint. J.
- 709 Phys. Oceanogr., 35, 1891-1910.
- Ferreira, D., J. Marshall, and B. Rose, 2011: Climate determinism revisited: multiple equilibria in a complex climate model. *J. Climate*, **24**, 992–1012.
- Frankignoul, C. and K. Hasselmann, 1977: Stochastic climate models. Part II: Application to sea-surface temperature variability and thermocline variability. *Tellus*, **29**, 284–305.
- Frankignoul, C., E. Kestenare, M. Botzet, A. F. Carril, H. Drange, A. Pardaens, L. Terray, and R. Sutton, 2004: An intercomparison between the surface heat flux feedback in five coupled models, COADS and the NCEP reanalysis. *Climate Dyn.*, **22**, 373–388.
- Gent, P. R. and J. C. McWilliams, 1990: Isopycnic mixing in ocean circulation models. *J. Phys. Oceanogr.*, **20**, 150–155.
- Gent, P. R., S. G. Yeager, R. B. Neale, S. Levis, and D. A. Bailey, 2010: Improvements in half degree atmosphere/land version of the CCSM. *Climate Dyn.*, **34**, 819–833.
- Gillet, N. P. and D. W. J. Thompson, 2003: Simulation of recent southern hemisphere climate change. *Science*, **302**, 273–275.

- Goosse, H., W. Lefebvre, A. de Montety, E. Crespin, and A. H. Orsi, 2009: Consistent past
- half-century trends in the atmosphere, the sea ice and the ocean at high southern latitudes.
- 725 Climate Dyn., **33**, 999–1016.
- Grise, K. M., L. M. Polvani, G. Tselioudis, Y. Wu, and M. D. Zelinka, 2013: The ozone
- hole indirect effect: Cloud-radiative anomalies accompanying the poleward shift of the
- eddy-driven jet in the southern hemisphere. Geophys. Res. Lett., 40, 3688–3692.
- Hall, A. and M. Visbeck, 2002: Synchronous variability in the southern hemisphere atmo-
- sphere, sea ice, and ocean resulting from the annular mode. J. Climate, 15, 3043–3057.
- Hallberg, R. and A. Gnanadesikan, 2006: The role of eddies in determining the structure and
- response of the wind-driven southern hemisphere overturning: Results from the modeling
- eddies in the southern ocean (MESO) project. J. Phys. Oceanogr., 36, 2232–2252.
- Kiehl, J. T., T. L. Schneider, R. W. Portmann, and S. Solomon, 1999: Climate forcing due
- to tropospheric and statospheric ozone. J. Geophys. Res., 104, 31,239–31,254.
- Kirtman, B. P., et al., 2012: Impact of ocean model resolution on CCSM climate simulations.
- 737 Climate Dyn., **39**, 1303–1328.
- Klinger, B. A., J. Marshall, and U. Send, 1996: Representation of convective plumes by
- vertical adjustment. J. Geophys. Res., C8 (101), 18,175–18,182.
- Knutti, R., et al., 2008: A review of uncertainties in global temperature projections over the
- twenty-first century. *J. Climate*, **21**, 2651–2663.
- Lefebvre, W. and H. Goosse, 2008: Analysis of the projected regional sea-ice changes in the
- southern ocean during the twenty-first century. Climate Dyn., 30, 59–76.
- Lefebvre, W., H. Goosse, R. Timmermann, and T. Fichefet, 2004: Influence of the southern
- annular mode on the sea-ice system. J. Geophys. Res., 109, C09 005.

- Marshall, G. J., 2003: Trends in the southern annular mode from observations and reanalysis.
- J. Climate, **16**, 4134–4143.
- Marshall, G. J., P. A. Stott, J. Turner, W. B. Connolley, J. C. King, and T. A. Lachlan-Cope,
- ⁷⁴⁹ 2004a: Causes of exceptional atmospheric circulation changes in the southern hemisphere.
- 750 Geophys. Res. Lett., **31**, L14 205.
- Marshall, J., A. Adcroft, J.-M. Campin, C. Hill, and A. White, 2004b: Atmosphere-ocean
- modeling exploiting fluid isomorphisms. Mon. Wea. Rev., 132, 2882–2894.
- Marshall, J., A. Adcroft, C. Hill, L. Perelman, and C. Heisey, 1997a: A finite-volume,
- incompressible navier stokes model for studies of the ocean on parallel computers. J.
- Geophys. Res., 102 (C3), 5753-5766.
- Marshall, J., K. C. Armour, J. R. Scott, Y. Kostov, U. Hausmann, D. Ferreira, T. G.
- Shepherd, and C. M. Bitz, 2014: The ocean's role in polar climate change: asymmetric
- arctic and antarctic responses to greenhouse gas and ozone forcing. Phil. Trans. R. Soc.
- A., In press.
- Marshall, J., D. Ferreira, J. Campin, and D. Enderton, 2007: Mean climate and variability
- of the atmosphere and ocean on an aquaplanet. J. Atmos. Sci., 64, 4270–4286.
- Marshall, J., C. Hill, L. Perelman, and A. Adcroft, 1997b: Hydrostatic, quasi-hydrostatic,
- and nonhydrostatic ocean modeling. J. Geophys. Res., 102 (C3), 5733–5752.
- Marshall, J. and T. Radko, 2003: Residual mean solutions for the antarctic circumpolar
- current and its associated overturning circulation. J. Phys. Oceanogr., 33, 2341–2354.
- Molteni, F., 2003: Atmospheric simulations using a GCM with simplified physical
- parametrizations. I: model climatology and variability in multi-decadal experiments. Cli-
- 768 mate Dyn., **64**, 175–191.

- Morrison, A. K. and A. M. Hogg, 2013: On the relationship between southern ocean overturning and acc transport. *J. Phys. Oceanogr.*, **43**, 140–148.
- Parkinson, C. L. and D. J. Cavalieri, 2012: Antarctic sea ice variability and trends, 1979–2010. The Cryosphere, 6, 871–880.
- Polvani, L. M., D. W. Waugh, G. J. P. Correa, and S.-W. Son, 2011: Stratospheric ozone depletion: the main driver of twentieth-century atmospheric circulation changes in the southern hemisphere. *J. Climate*, **24**, 795–812.
- Previdi, M. and L. M. Polvani, 2014: Climate system response to stratospheric ozone depletion and recovery. *Quart. J. Roy. Meteor. Soc.*
- Redi, M. H., 1982: Oceanic isopycnal mixing by coordinate rotation. *J. Phys. Oceanogr.*, **12**, 1154–1158.
- Sallée, J. B., K. G. Speer, and S. R. Rintoul, 2010: Zonally asymmetric response of the southern ocean mixed-layer depth to the southern annular mode. *Nature Geoscience*, **3**, 273–279.
- Sen Gupta, A. and M. H. England, 2006: Coupled ocean-atmosphere-ice response to variations in the southern annular mode. *J. Climate*, **19**, 4457–4486.
- Sigmond, M. and J. C. Fyfe, 2010: Has the ozone hole contributed to increased antarctic sea ice extent? *Geophys. Res. Lett.*, **37**, L18 502.
- Sigmond, M. and J. C. Fyfe, 2014: The antarctic sea ice response to the ozone hole in climate models. *J. Climate*, **27**, 1336–1342.
- Sigmond, M., J. C. Fyfe, and J. F. Scinocca, 2010: Does the ocean impact the atmospheric response to stratospheric ozone depletion? *Geophys. Res. Lett.*, **37**, L12706.

- Simpkins, G. R., L. M. Ciasto, D. W. J. Thompson, and M. H. England, 2012: Seasonal
- relationships between large-scale climate variability and antarctic sea ice concentration.
- 793 J. Climate, **25**, 5451–5469.
- Smith, K. L., L. M. Polvani, and D. R. Marsh, 2012: Mitigation of 21st century antarctic
- sea ice loss by stratospheric ozone recovery. Geophys. Res. Lett., 39, L20 701.
- Solomon, S., R. W. Portmann, and D. W. J. Thompson, 2007: Constrast between antarctic
- and arctic ozone depletion. Proc. Natl. Acad. Sci., 104 (2), 445–449.
- Son, S.-W., et al., 2010: Impact of stratospheric ozone on southern hemisphere circulation
- change: A multimodel assessment. J. Geophys. Res., 115 (D3(16)), D00M07.
- Thompson, D. W. J. and S. Solomon, 2002: Interpretation of recent southern hemisphere
- climate change. *Science*, **296**, 895–899.
- Thompson, D. W. J., S. Solomon, P. J. Kushner, M. H. England, K. M. Grise, and D. J.
- Karoly, 2011: Signatures of the antarctic ozone hole in southern hemisphere surface climate
- change. Nature Geoscience.
- Turner, J., et al., 2009: Non-annular atmospheric circulation change induced by stratospheric
- ozone depletion and its role in the recent increase of antarctic sea ice extent. Geophys.
- 807 Res. Lett., **36**, L08 502.
- Watterson, I. G., 2000: Southern midlatitude zonal wind vacillation and its interaction with
- the ocean in gcm simulations. J. Climate, 13, 562–578.
- Winton, M., 2000: A reformulated three-layer sea ice model. J. Atmos. Oceanic Technol.,
- 811 **17**, 525–531.
- Zwally, H. J., J. C. Comiso, C. L. Parkinson, D. J. Cavalieri, and P. Gloersen, 2002: Vari-
- ability of antarctic sea ice 1979–1998. J. Geophys. Res., 107, 3041.

List of Tables

1 Parameters of the simple model estimated by fitting Eqs. (8) and (9) to the 815 SST and subsurface temperature time series diagnosed in the MITgcm and 816 CCSM3.5 (h_s =30 m). The model time series and fitted curves are shown 817 in Fig. 15. The temperatures responses are averaged over 70-50°S for the 818 MITgcm and over the initial cold SST response for CCSM3.5. Note that 819 λ_F and \tilde{F}_F are the same physical quantities as λ and \tilde{F} but expressed in 820 W m⁻² K⁻¹ and W m⁻² respectively, assuming a mixed layer depth h_s of 821 30 m for both models. 822

TABLE 1. Parameters of the simple model estimated by fitting Eqs. (8) and (9) to the SST and subsurface temperature time series diagnosed in the MITgcm and CCSM3.5 (h_s =30 m). The model time series and fitted curves are shown in Fig. 15. The temperatures responses are averaged over 70-50°S for the MITgcm and over the initial cold SST response for CCSM3.5. Note that λ_F and \tilde{F}_F are the same physical quantities as λ and \tilde{F} but expressed in W m⁻² K⁻¹ and W m⁻² respectively, assuming a mixed layer depth h_s of 30 m for both models.

	Air-sea damping		Atm. forcing		λ_{sub}^{-1}	Λ_e^{-1}	$-w_{res}^{\prime}\partial_{z}\overline{T}_{sub}$
	λ^{-1}	λ_F	$ ilde{F}$	$ ilde{F}_F$			
	year	${ m W} { m m}^{-2} { m K}^{-1}$	$^{\circ}\mathrm{C}~\mathrm{year^{-1}}$	${ m W~m^{-2}}$	year	year	°C year ⁻¹
MITgcm	2.6	1.5	-0.18	-0.7	78	1.5	0.014
CCSM3.5	0.59	6.7	-0.27	-1.1	6.8	0.36	0.027

List of Figures

844

846

847

848

- 1 Schematic of the two-timescale response of the ocean and sea ice to an abrupt 824 ozone depletion, capturing the common features of the two GCMs: (left) the 825 fast response, similar to the signature of the interannual SAM seen in obser-826 vations, is dominated by the surface dynamics and (right) the slow response, 827 seen in coupled GCMs, is driven by the ocean interior dynamics. Black arrows 828 denote anomalous ocean currents. Red/blue arrows denote heat fluxes in/out 829 of the surface mixed layer (marked by a thick dashed line). Blue patches 830 represent the sea ice cover (expanding in the fast response and contracting in 831 the slow response). The thin dashed lines mimic the structure of isotherms in 832 the Southern Ocean, showing in particular the temperature inversion found 833 south of the ACC. 40 834 2 Response of the geopotential height at 500 mb to an abrupt ozone depletion in 835 the MITgcm (in meters): (left) in DJF and (right) zonal mean climatological 836 response. The time average is over the first 20 years. 41 837 Annual- and zonal-mean response of the surface wind stress (N m⁻²) to an 3 838 abrupt ozone depletion in the MITgcm (dashed) and in CCSM3.5 (dashed-839 dotted). The time average is over the first 20 years. For comparison, the 840 surface wind stress pattern of the SAM in the NCEP-NCAR re-analysis is 841 shown in solid (the magnitude corresponds to a third of one standard deviation 842 of the SAM). 42 843
 - 4 Response of atmosphere to an abrupt ozone depletion in the CCSM3.5: (left) response of the geopotential height (meter) at 500 mb in DJF, (right top) zonal mean climatological response of the geopotential height at 500 mb and (right bottom) the annual mean zonal mean wind stress response (black) (the control wind stress in shown in grey).

43

- Response of (left) SST (°C) and surface wind (m s⁻¹) and (right) potential temperature at 170 m averaged over years 1-5 (top) and 16-20 (bottom) after "Ozone Hole" inception in the MITgcm.
- 852 6 Zonal mean SST response in the MITgcm (monthly means, in °C). 45

44

46

47

48

49

- 7 Time evolution of the annual-mean ensemble-mean SST response (red) in 853 (left) the MITgcm and (right) CCSM3.5. Solid lines correspond to an average 854 between 70 and 50°S. In addition, for CCSM3.5, an average over the area 855 occupied by the cold pole of the first year response (see Fig. 13 top, below) 856 is shown with dotted lines. The solid black line indicates the mean of the 857 best fitted curves while the grey shading denotes uncertainties (see text for 858 details). For the MITgcm, a 20 member-ensemble is used over the 40 years. 859 For CCSM3.5, a 20-member ensemble mean is only available for the first 3 860 years, after which only the ensemble mean comprises 6 members. 861
- Sea ice cover response (in 10⁶ km²) as a function of time in summer (January-March, red) and winter (August-October, black) in (left) the MITgcm and (right) CCSM3.5. Note that CCSM3.5 starts in September, so the first winter is an average of September-October only.
- Response of zonal mean SST (°C, red), net air-sea flux F'_F (W m⁻², solid black) and horizontal advection at the surface $-\rho_o c_p h_s v'_{res} \partial_y \overline{T}$ (W m⁻², dasheddotted black) with h_s =30 m. Fluxes are counted positive if they result in an SST increase. Results are shown for the MITgcm experiment on the left (averaged over years 2-3) and on the right for CCSM3.5 (averaged over months 5-28). Note the different vertical scales in the two panels.
- 10 (Top) Annual mean surface wind stress response (N m²). (bottom) Annual
 mean Eulerian MOC response (Sv, black) and potential temperature distribution in the control run (°C, color). The responses are averaged over years
 6-10.

sponse (color) averaged over five year periods. The contour interval for the
MOC are ±0.5, ±1, ±2 Sv, etc ... Clockwise and anticlockwise circulations
are denoted by solid and dashed lines, respectively. (d) Time series of potential temperature (black) averaged over the box shown in panel a). The
best fit slope (dashed) equals 0.017°C/year. The grey shading indicates the
magnitude of the fast (cold) SST response around 60°S.

- (Top) Eulerian (circle) and residual-mean (cross) vertical velocities (m year⁻¹) averaged over the latitudinal bands dominated by upwelling (blue) and down-welling (red) and (bottom) subsurface vertical advection tendencies $-w'_{res} \frac{\partial \overline{T}}{\partial z}$ (°C year⁻¹). The left and right plots correspond to the MITgcm and CCSM3.5, respectively. Note that the boundaries of the latitudinal bands (top) and depths at which vertical advection peaks (bottom) vary between models as indicated by insets. Note also that, in the bottom plots, the vertical scale for CCSM3.5 is larger than for MITgcm.
- Response of SST (°C) averaged over the first year (top) and years 11-20 (bottom) after an abrupt ozone depletion in the CCSM3.5.

- Zonal mean SST response in CCSM3.5 (monthly means, in °C). The vertical line separates the first 32 months when 20 ensemble members are averaged from the later months where just 6 ensemble members are averaged.
- Best-fit (solid blue) of Eq. (8) to the CFR of the SST evolution (red, averaged over 70-50°S for the MITgcm and over the initial cold SST response for CCSM3.5) in (left) the MITgcm and (right) CCSM3.5. The slow and fast components of the best fit are shown in dashed lines.

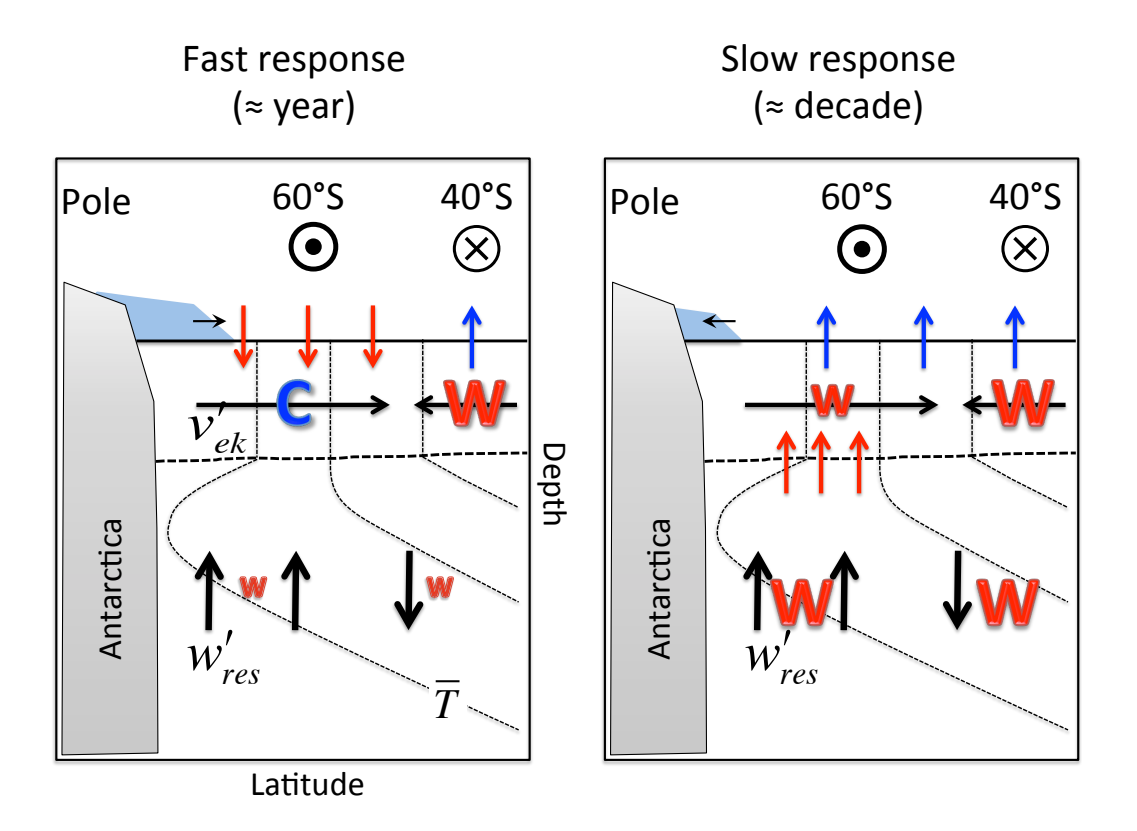


Fig. 1. Schematic of the two-timescale response of the ocean and sea ice to an abrupt ozone depletion, capturing the common features of the two GCMs: (left) the fast response, similar to the signature of the interannual SAM seen in observations, is dominated by the surface dynamics and (right) the slow response, seen in coupled GCMs, is driven by the ocean interior dynamics. Black arrows denote anomalous ocean currents. Red/blue arrows denote heat fluxes in/out of the surface mixed layer (marked by a thick dashed line). Blue patches represent the sea ice cover (expanding in the fast response and contracting in the slow response). The thin dashed lines mimic the structure of isotherms in the Southern Ocean, showing in particular the temperature inversion found south of the ACC.

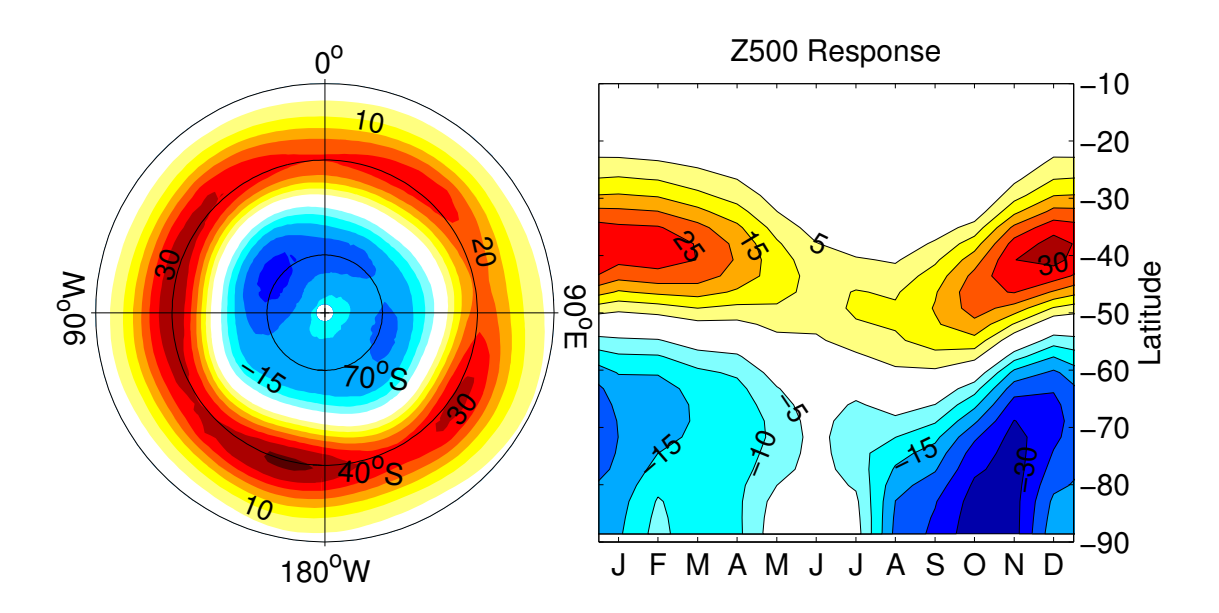


FIG. 2. Response of the geopotential height at 500 mb to an abrupt ozone depletion in the MITgcm (in meters): (left) in DJF and (right) zonal mean climatological response. The time average is over the first 20 years.

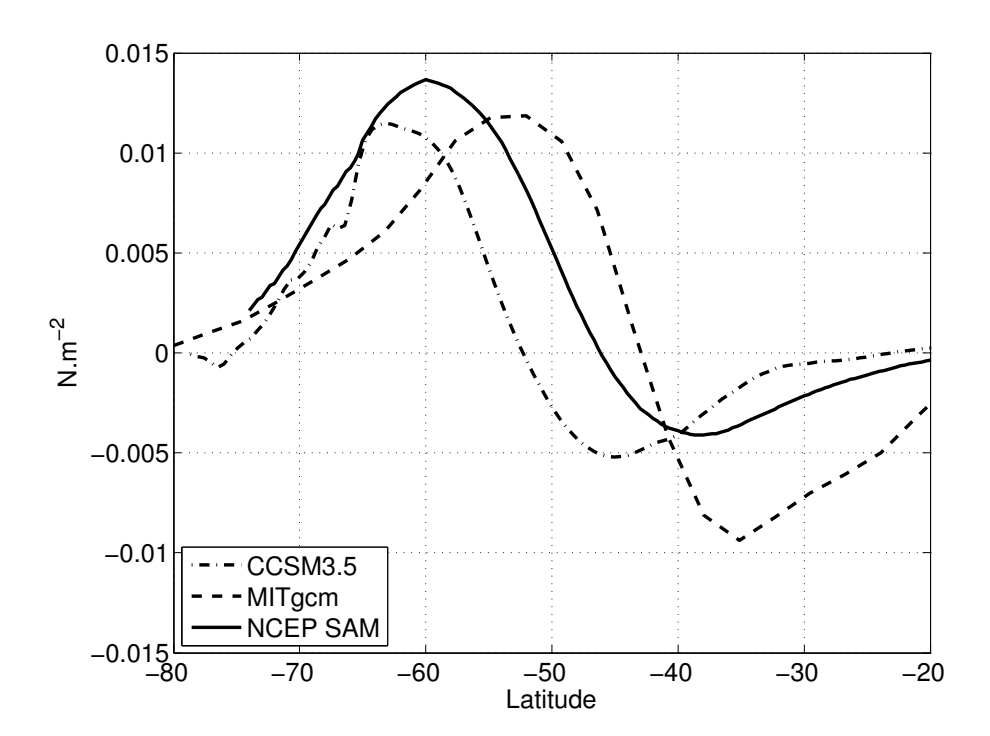


FIG. 3. Annual- and zonal-mean response of the surface wind stress (N $\rm m^{-2}$) to an abrupt ozone depletion in the MITgcm (dashed) and in CCSM3.5 (dashed-dotted). The time average is over the first 20 years. For comparison, the surface wind stress pattern of the SAM in the NCEP-NCAR re-analysis is shown in solid (the magnitude corresponds to a third of one standard deviation of the SAM).

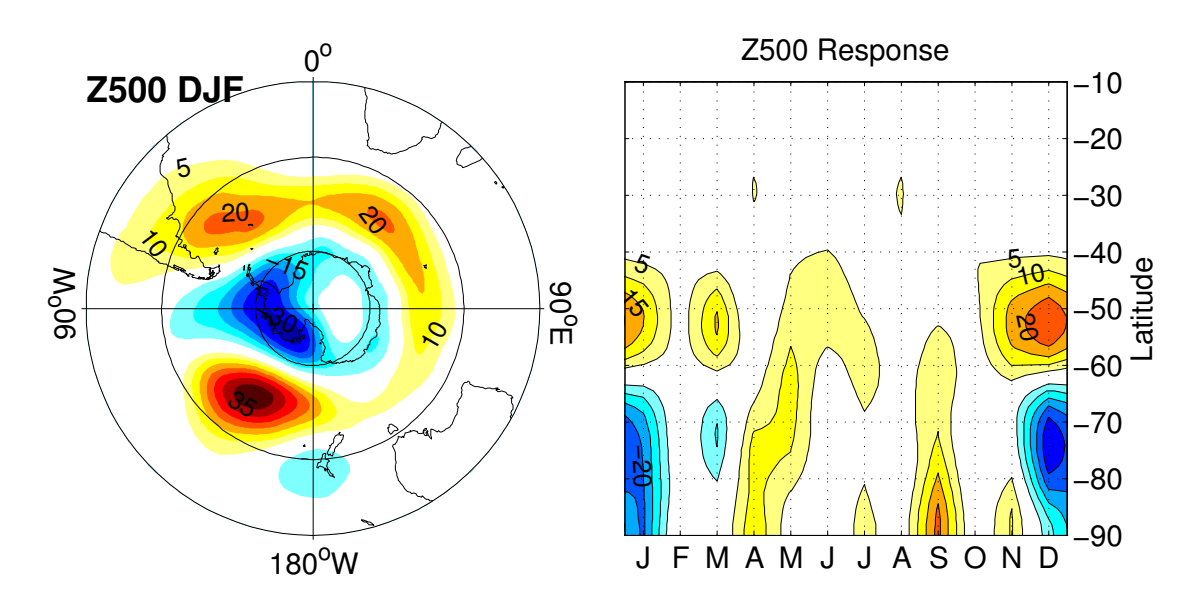


FIG. 4. Response of atmosphere to an abrupt ozone depletion in the CCSM3.5: (left) response of the geopotential height (meter) at 500 mb in DJF, (right top) zonal mean climatological response of the geopotential height at 500 mb and (right bottom) the annual mean zonal mean wind stress response (black) (the control wind stress in shown in grey).

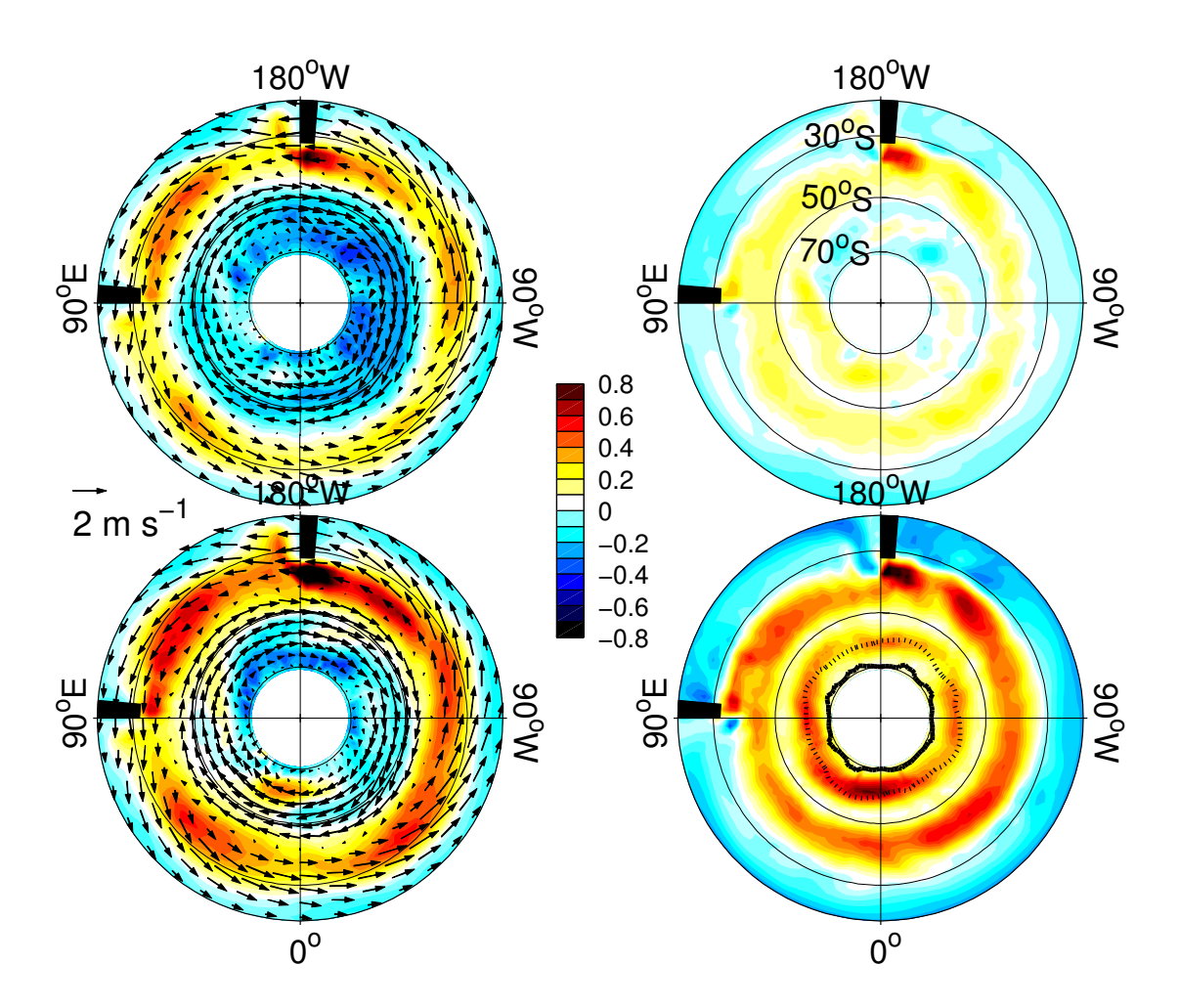


FIG. 5. Response of (left) SST (°C) and surface wind (m $\rm s^{-1}$) and (right) potential temperature at 170 m averaged over years 1-5 (top) and 16-20 (bottom) after "Ozone Hole" inception in the MITgcm.

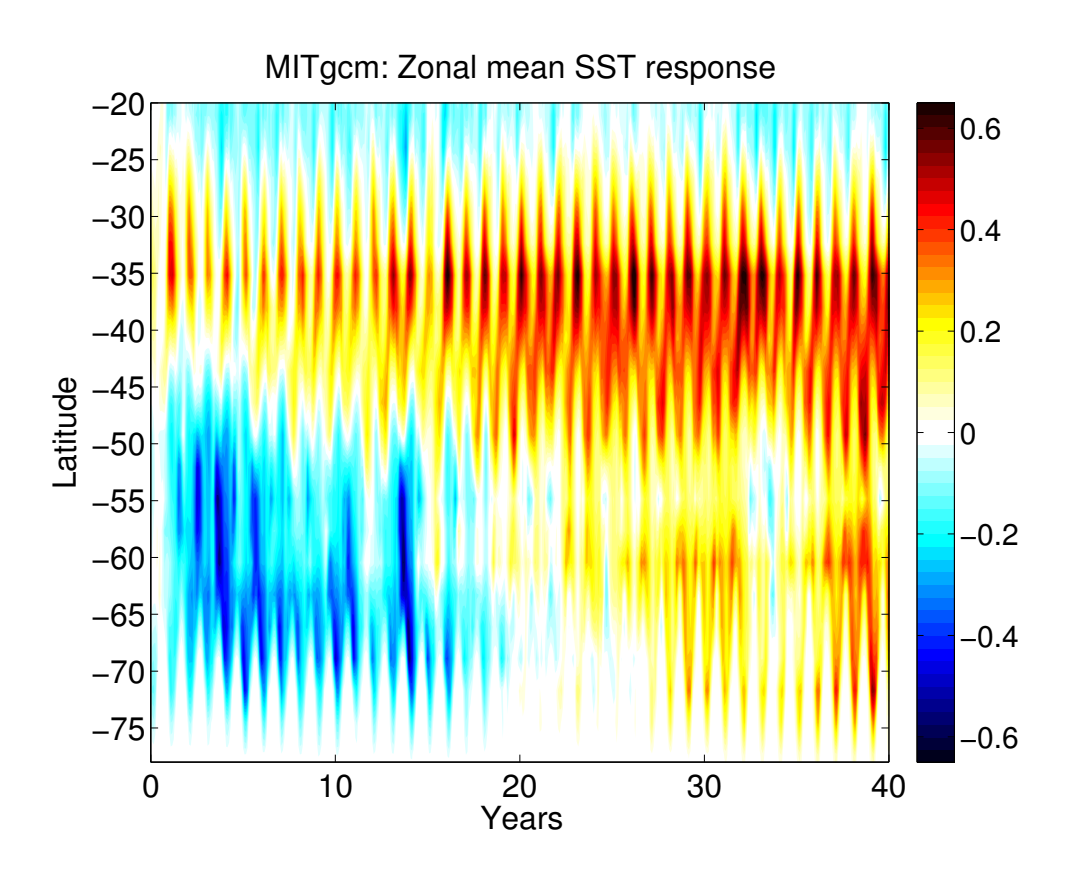


Fig. 6. Zonal mean SST response in the MITgcm (monthly means, in $^{\circ}\mathrm{C}).$

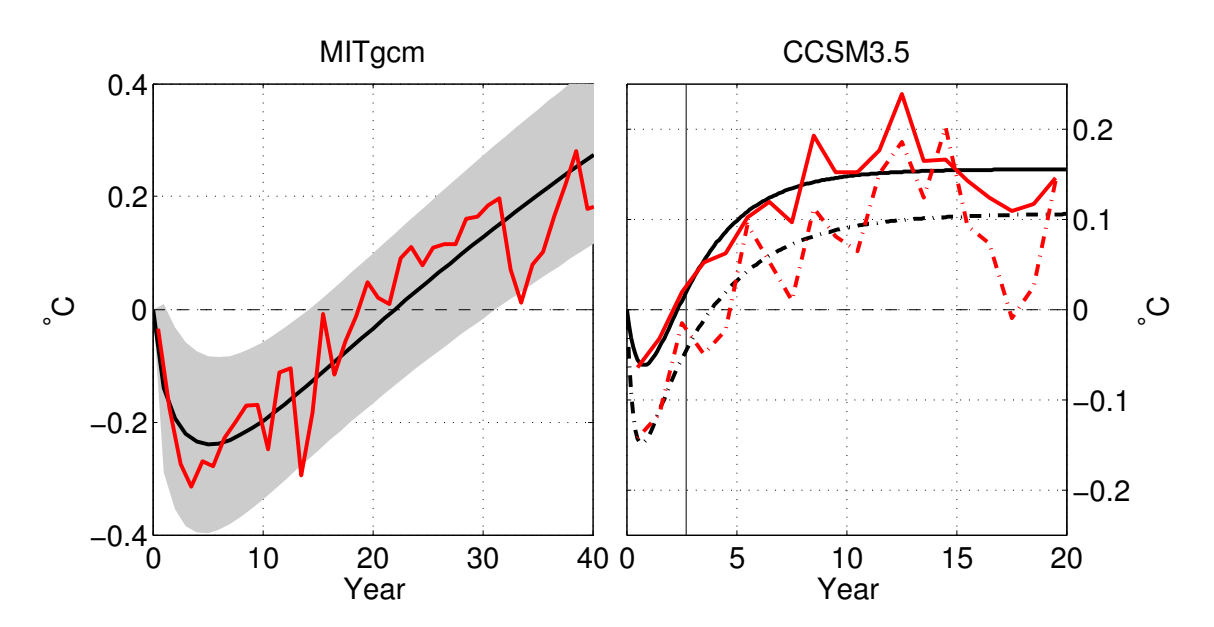


FIG. 7. Time evolution of the annual-mean ensemble-mean SST response (red) in (left) the MITgcm and (right) CCSM3.5. Solid lines correspond to an average between 70 and 50°S. In addition, for CCSM3.5, an average over the area occupied by the cold pole of the first year response (see Fig. 13 top, below) is shown with dotted lines. The solid black line indicates the mean of the best fitted curves while the grey shading denotes uncertainties (see text for details). For the MITgcm, a 20 member-ensemble is used over the 40 years. For CCSM3.5, a 20-member ensemble mean is only available for the first 3 years, after which only the ensemble mean comprises 6 members.

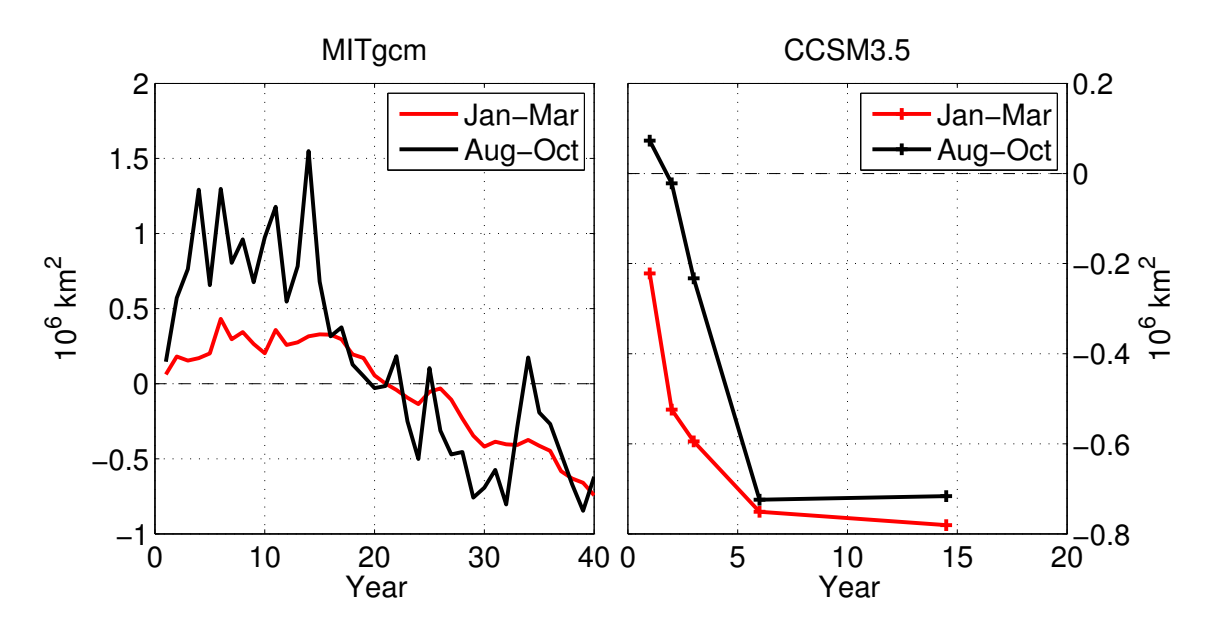


FIG. 8. Sea ice cover response (in $10^6 \,\mathrm{km^2}$) as a function of time in summer (January-March, red) and winter (August-October, black) in (left) the MITgcm and (right) CCSM3.5. Note that CCSM3.5 starts in September, so the first winter is an average of September-October only.

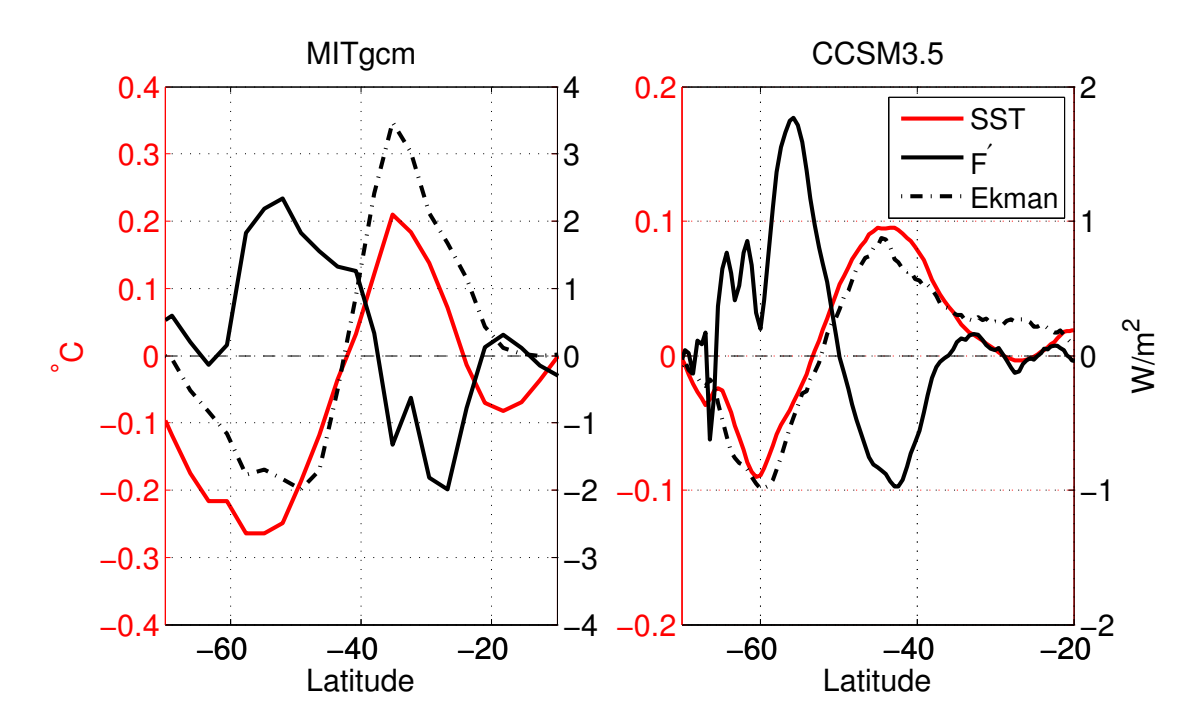


FIG. 9. Response of zonal mean SST (°C, red), net air-sea flux F_F' (W m⁻², solid black) and horizontal advection at the surface $-\rho_o c_p h_s v_{res}' \partial_y \overline{T}$ (W m⁻², dashed-dotted black) with h_s =30 m. Fluxes are counted positive if they result in an SST increase. Results are shown for the MITgcm experiment on the left (averaged over years 2-3) and on the right for CCSM3.5 (averaged over months 5-28). Note the different vertical scales in the two panels.

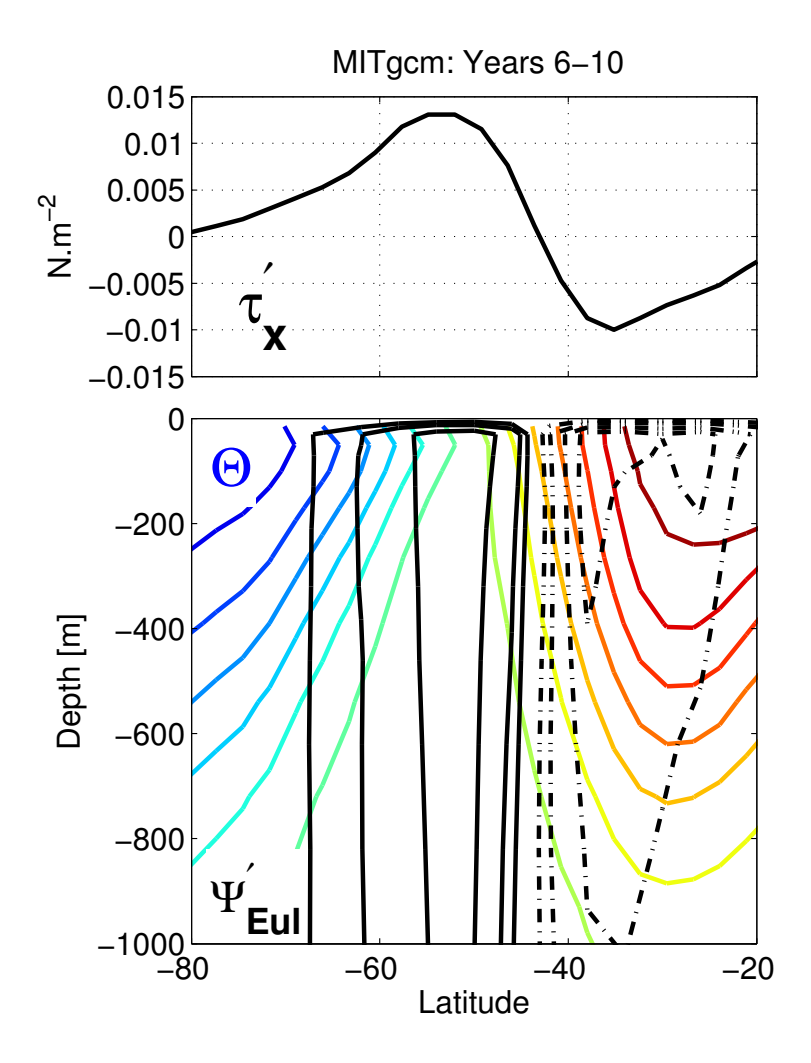


Fig. 10. (Top) Annual mean surface wind stress response (N $\rm m^2$). (bottom) Annual mean Eulerian MOC response (Sv, black) and potential temperature distribution in the control run (°C, color). The responses are averaged over years 6-10.

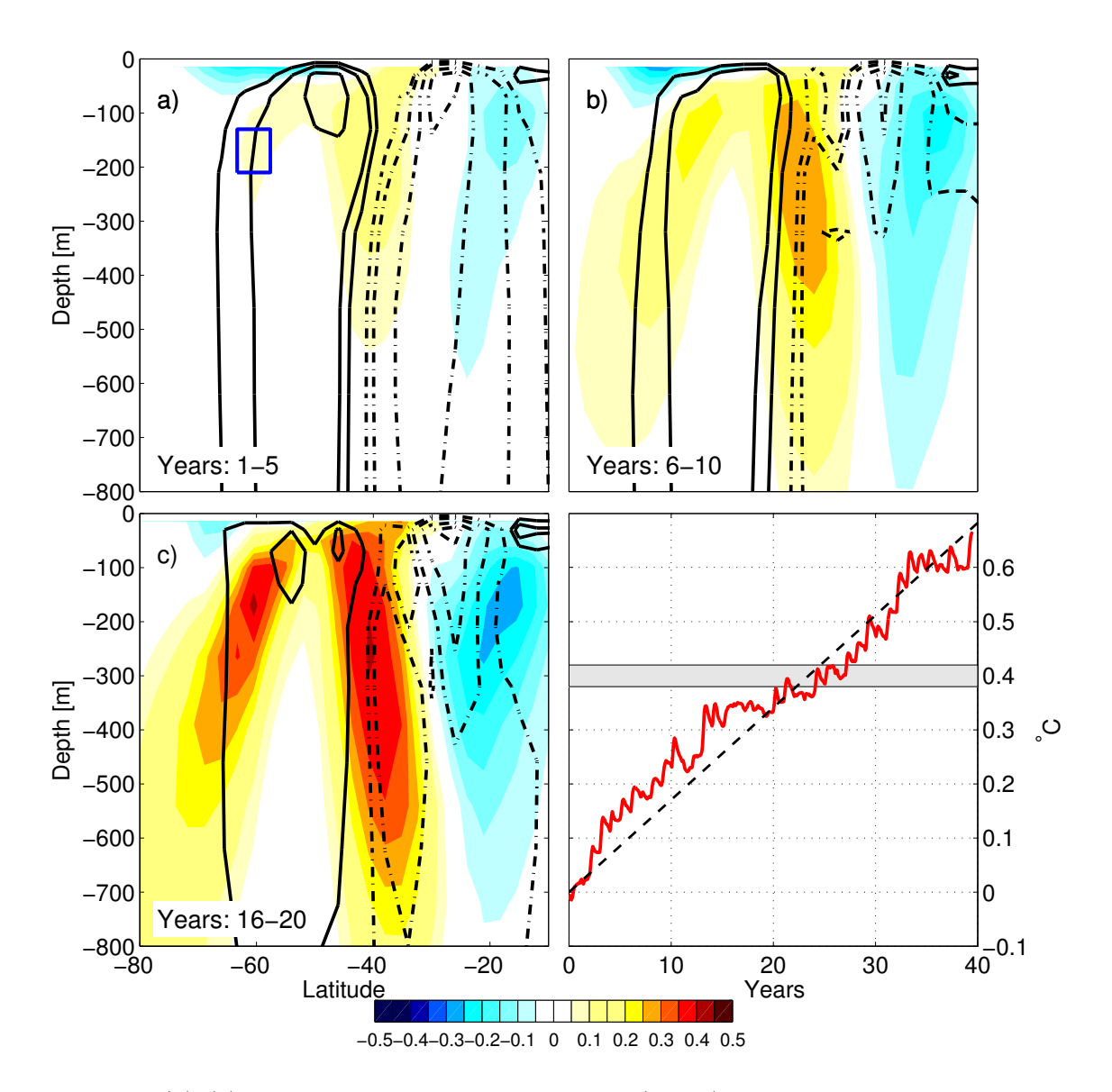


Fig. 11. (a)-(c): Residual-mean MOC response (black) and potential temperature response (color) averaged over five year periods. The contour interval for the MOC are ± 0.5 , ± 1 , ± 2 Sv, etc... Clockwise and anticlockwise circulations are denoted by solid and dashed lines, respectively. (d) Time series of potential temperature (black) averaged over the box shown in panel a). The best fit slope (dashed) equals 0.017° C/year. The grey shading indicates the magnitude of the fast (cold) SST response around 60° S.

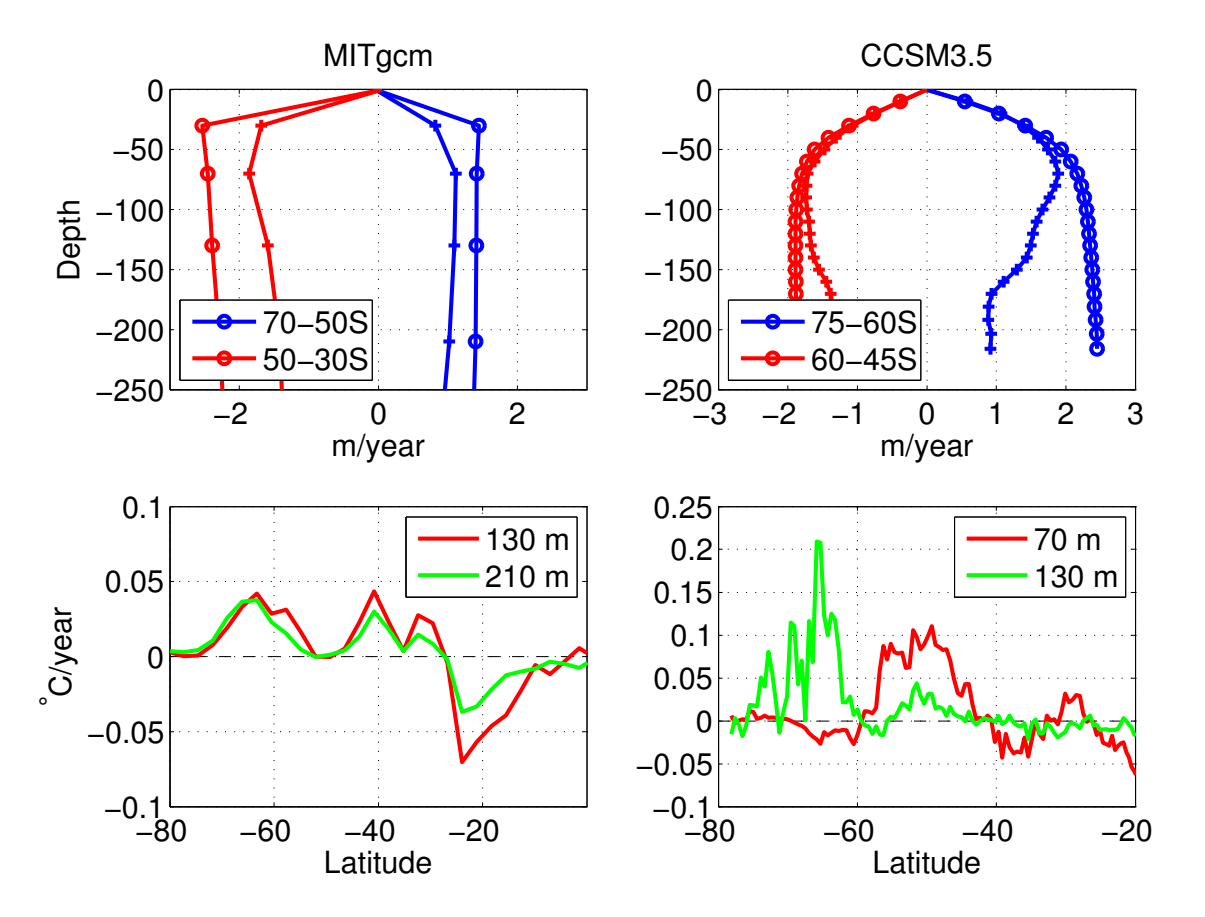


FIG. 12. (Top) Eulerian (circle) and residual-mean (cross) vertical velocities (m year⁻¹) averaged over the latitudinal bands dominated by upwelling (blue) and downwelling (red) and (bottom) subsurface vertical advection tendencies $-w'_{res} \frac{\partial \overline{T}}{\partial z}$ (°C year⁻¹). The left and right plots correspond to the MITgcm and CCSM3.5, respectively. Note that the boundaries of the latitudinal bands (top) and depths at which vertical advection peaks (bottom) vary between models as indicated by insets. Note also that, in the bottom plots, the vertical scale for CCSM3.5 is larger than for MITgcm.

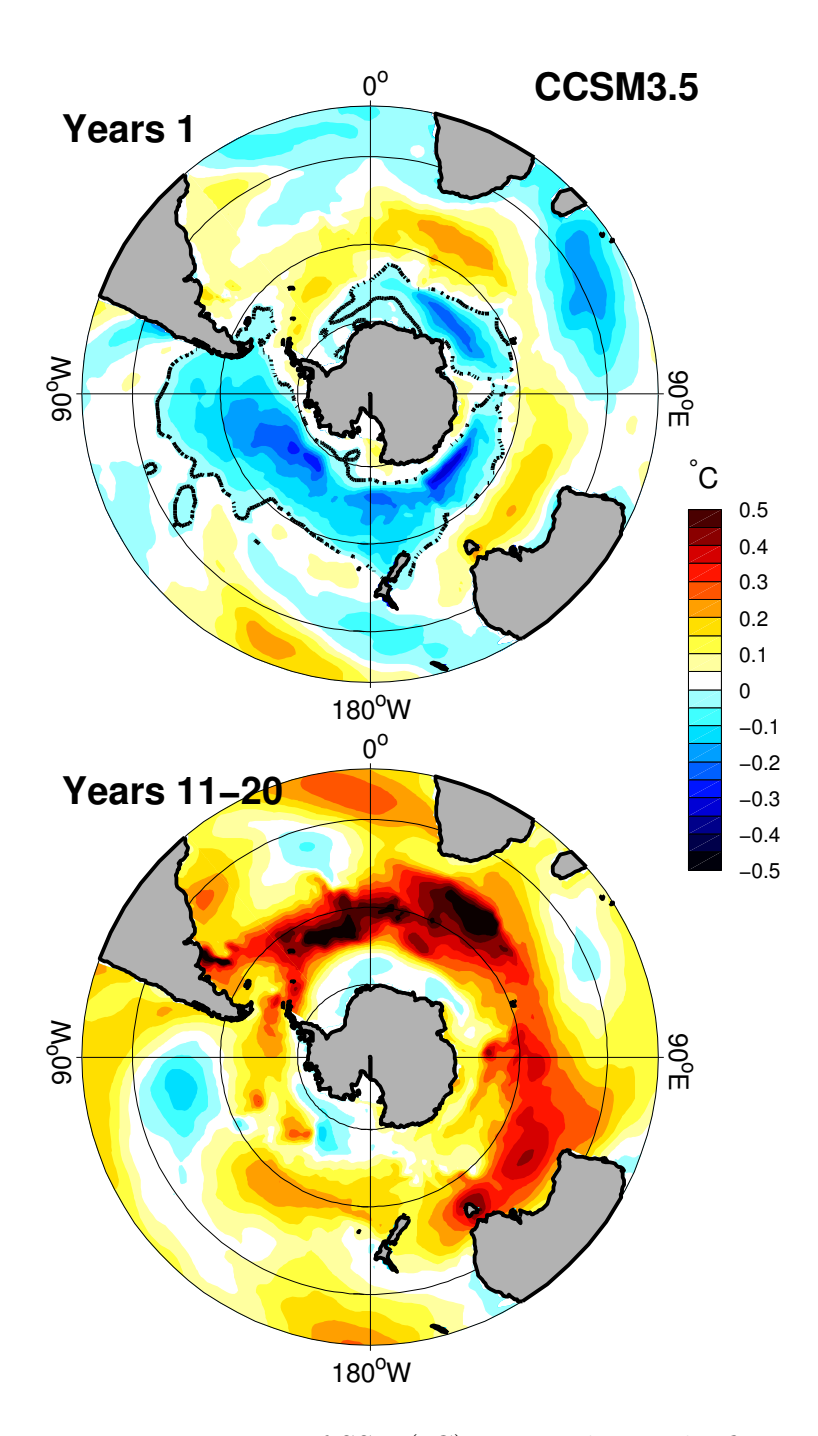


Fig. 13. Response of SST (°C) averaged over the first year (top) and years 11-20 (bottom) after an abrupt ozone depletion in the CCSM3.5.

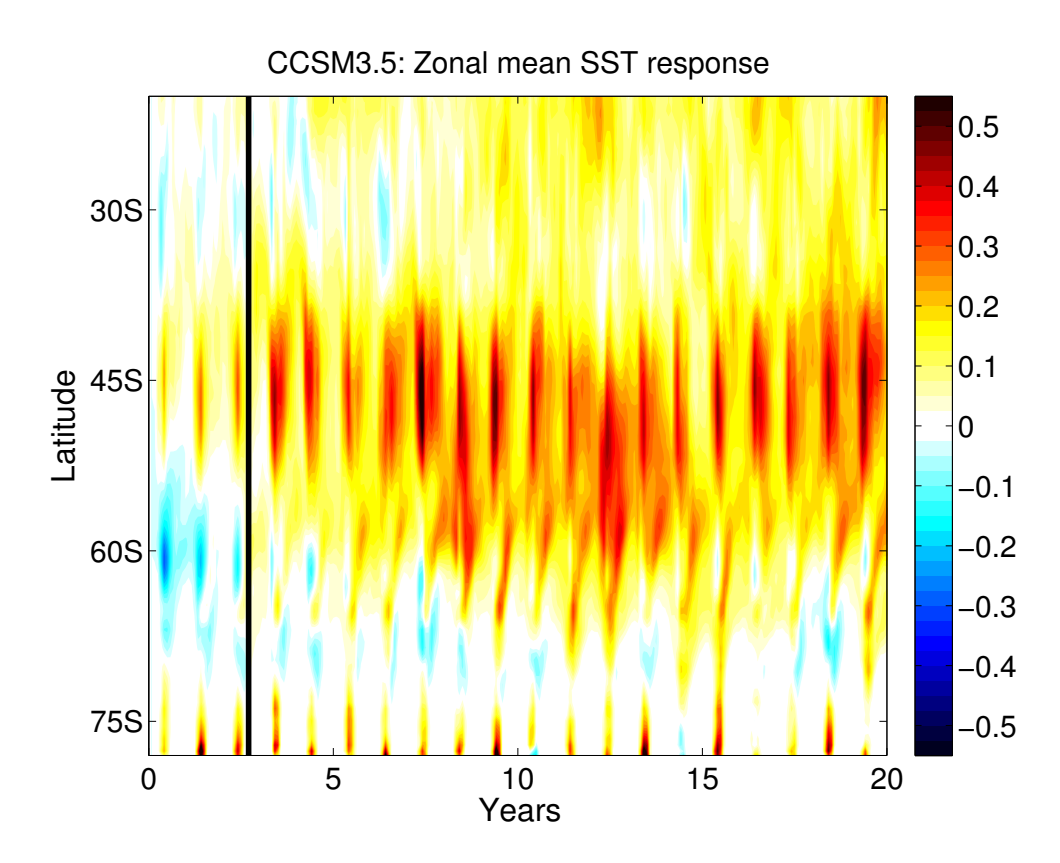


Fig. 14. Zonal mean SST response in CCSM3.5 (monthly means, in $^{\circ}$ C). The vertical line separates the first 32 months when 20 ensemble members are averaged from the later months where just 6 ensemble members are averaged.

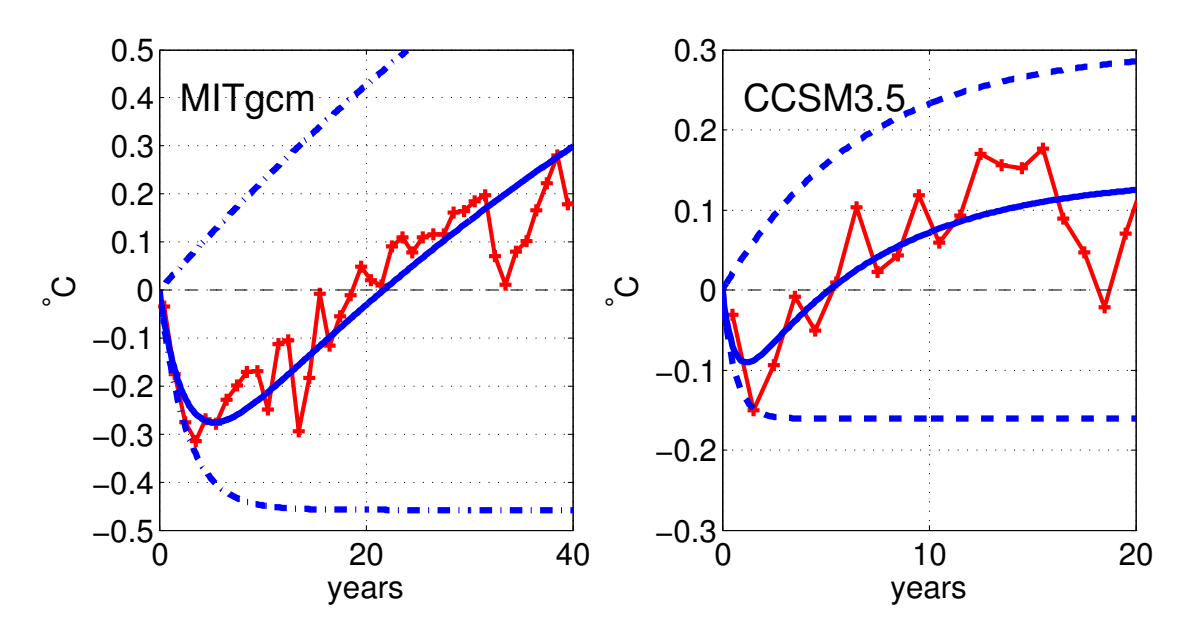


FIG. 15. Best-fit (solid blue) of Eq. (8) to the CFR of the SST evolution (red, averaged over 70-50°S for the MITgcm and over the initial cold SST response for CCSM3.5) in (left) the MITgcm and (right) CCSM3.5. The slow and fast components of the best fit are shown in dashed lines.